Eur. Phys. J. A **17**, 537–558 (2003)
DOI 10.1140/epja/i2002-10162-1

THE EUROPEAN PHYSICAL JOURNAL A

Alpha-decay studies of the new isotopes ^{191}At and ^{193}At

H. Kettunen[a], T. Enqvist, T. Grahn, P.T. Greenlees, P. Jones, R. Julin, S. Juutinen, A. Keenan, P. Kuusiniemi, M. Leino, A.-P. Leppänen, P. Nieminen, J. Pakarinen, P. Rahkila, and J. Uusitalo

Department of Physics, University of Jyväskylä, P.O. Box 35, FIN-40014 Jyväskylä, Finland

Received: 16 December 2002 / Revised version: 26 March 2003 /
Published online: 4 August 2003 –
Communicated by C. Signorini

Abstract. Detailed alpha-decay studies have been performed for the neutron-deficient isotopes ^{191}At and ^{193}At. The nuclei were produced in fusion-evaporation reactions of ^{54}Fe and ^{56}Fe ions with a ^{141}Pr target. The fusion products were separated in-flight using a gas-filled recoil separator and implanted into a position-sensitive silicon detector. The isotopes were identified using position, time and energy correlations between the implants and subsequent alpha-decays. Three alpha-decaying states were identified for ^{193}At and two for ^{191}At. The spin and parity of the initial states in the astatine isotopes were deduced based on unhindered alpha-decays to states in the bismuth daughter nuclei. In both astatine isotopes the $1/2^+$ intruder state was determined to be the ground state and a $7/2^-$ state to be the first-excited state. In ^{193}At the alpha-decay of the $13/2^+$ state was observed in coincidence with a previously known gamma-ray transition from the $13/2^+$ state in the corresponding daughter nucleus ^{189}Bi. In ^{187}Bi and ^{189}Bi low-lying $7/2^-$ states were observed for the first time via alpha-decay of the mother nuclei.

PACS. 23.60.+e Alpha decay – 27.80.+w $190 \leq A \leq 219$ – 23.20.Lv γ transitions and level energies – 21.10.Dr Binding energies and masses

1 Introduction

The region of neutron-deficient nuclei far from stability around the closed $Z = 82$ proton shell offers an interesting challenge for various theoretical models as well as experimental instruments. An amazing variety of different nuclear phenomena can be observed in this very limited region of the nuclear chart. The great selection of phenomena can be understood by the coupling of the particles and particle holes to the doubly magic ^{208}Pb core.

Currently, the coexistence of different shapes in an atomic nucleus is an enthusiastically studied topic in nuclear physics. The neutron-deficient lead region offers an excellent opportunity to study this phenomenon in the vicinity of the closed proton shell. The even-even platinum and mercury isotopes are dramatic examples of shape coexistence just below the $Z = 82$ proton shell closure [1]. The closed proton shell in lead nuclei favours a spherical ground state, coexisting with an excited oblate deformed configuration, associated with the excitation of a proton pair across the closed-shell gap. Multiparticle and multihole excitations, associated with strong prolate deformation, were predicted to occur at comparable excitation energy to the oblate deformed structure near the neutron mid-shell at $N = 104$ [2,3]. These specific conditions of this particular region of the nuclear chart afford the existence of probably unique triple coexistence of different nuclear shapes [4,5].

Competition between different shapes can also be seen in the neutron-deficient polonium isotopes. Experimental results indicate that the spherical ground state of heavier polonium isotopes transforms to a slightly oblate shape around ^{194}Po (the oblate configuration dominates in ^{192}Po and ^{190}Po) before a prolate deformed structure was supposed to dominate the ground state of ^{188}Po [6–8]. In a recent experiment the prolate deformed intruder configuration was observed to become yrast already above $I \geq 4\hbar$ in ^{190}Po [7]. The properties of neutron-deficient polonium isotopes are predicted by theoretical calculations in ref. [2].

One of the interesting tasks of the experiments for nuclei above the $Z = 82$ proton shell gap and below the $N = 126$ neutron shell gap is to search for a new region of ground-state oblate deformed nuclei predicted by theoretical calculations [9,10]. Presently available experimental facilities and recoil-decay tagging techniques [11,12] have made in-beam gamma-ray spectroscopic experiments possible in the vicinity of this region of the nuclear chart. Despite these highly sensitive and sophisticated experimental devices, no clear evidence of the region of ground-state deformed nuclei above polonium isotopes has been obtained.

[a] e-mail: heikki.kettunen@phys.jyu.fi

In radon isotopes ^{202}Rn is predicted to be the lightest nearly spherical isotope with quadrupole deformation of $\beta_2 = -0.10$ before the change in ground-state deformation takes place in ^{201}Rn with $\beta_2 = -0.20$ [9,10]. Experimentally this change in the quadrupole deformation has been investigated in even-mass radon isotopes down to ^{198}Rn using in-beam gamma-ray spectroscopic measurements [13–16]. Although a slight steepening in the decreasing of the excitation energy of the 2_1^+ state was observed starting from ^{200}Rn, no result consistent with theoretical predictions of a sizeable ground-state deformation was discovered even in ^{198}Rn [13]. On the other hand, the sudden fall of the excitation energies of higher-spin states (4_1^+ and 6_1^+) with decreasing neutron number in radon isotopes with $A \leq 200$ indicates that the spherical structures are crossed at higher spins by structures similar to the oblate intruder states in Po isotopes [17].

In the astatine isotopes an even more dramatic change in the ground-state deformation is predicted to occur between ^{199}At and ^{198}At isotopes. The quadrupole deformation is estimated to change from $\beta_2 = 0.08$ to $\beta_2 = -0.21$ according to Möller *et al.* [9]. In contradiction to the theoretical calculations, in-beam gamma-ray spectroscopic measurements of odd-mass isotopes from ^{209}At to ^{197}At [18–23] do not show clear evidence for ground-state deformation in the neutron-deficient astatine isotopes. However, the decreasing behaviour of the excitation energy of the $13/2^+$ state in ^{199}At and ^{197}At can be interpreted as an indication of increasing collectivity. This interpretation is supported by the observation of analogous systematics in the polonium isotopes, where the increase in ground-state deformation was interpreted to occur around ^{194}Po [6].

The low production rates of more neutron-deficient astatine isotopes in heavy-ion fusion reactions hinder in-beam gamma-ray spectroscopic measurements. At present, alpha- or proton decays provide the only viable tools to obtain spectroscopic information about these nuclei.

Based on recent alpha-decay studies, a dramatic change in the decay scheme systematics was proposed to occur in ^{195}At, when compared to the heavier odd-mass astatine isotopes [24]. The intruder $1/2^+$ state, having a $\pi(4p-1h)$ configuration, was observed to become the ground state. In the heavier odd-mass astatine isotopes, the ground state is the $9/2^-$ state with the $(\pi h_{9/2})^3$ configuration. Also a $7/2^-$ state rather than a $9/2^-$ state was suggested to be the first-excited state in ^{195}At. The emergence of the $7/2^-$ state over the $9/2^-$ state can be understood by assuming a change in deformation of this three-particle configuration between the ^{197}At and ^{195}At isotopes. As discussed above, no sizeable ground-state deformation was observed in ^{197}At. Thus, the last proton in the $\pi h_{9/2}$ orbital creates the $9/2^-$ ground state. If sufficient oblate deformation is assumed in ^{195}At, the $7/2^-[514]$ Nilsson proton state, originating predominantly from the $\pi h_{9/2}$ orbital at sphericity and having a mixed $\pi f_{7/2}/\pi h_{9/2}$ character at oblate deformations, becomes available for the 85th proton creating a $7/2^-$ state. It was concluded, that in ^{195}At the deformed three-particle configuration, driving the last proton to the $7/2^-[514]$ Nilsson state, becomes energetically more favoured than the nearly spherical $(\pi h_{9/2})^3$ configuration [24].

One motivation of the present work has been to study the decay schemes of light odd-mass astatine isotopes (^{191}At and ^{193}At) and investigate whether they are similar to the proposed decay scheme of ^{195}At [24].

Another aim of the experiment was the search for possible proton emission in the astatine isotopes. So far the heaviest known proton emitter is ^{185}Bi with $Z = 83$ [25, 26]. For ^{185}Bi the proton emission was observed from the $1/2^+$ intruder state and so far, no evidence for the decay of the $9/2^-$ state (ground state in heavier bismuth isotopes) has been observed. In ref. [26] it was speculated whether the $1/2^+$ state has become the ground state in ^{185}Bi. For all known proton emitters above the closed $N = 82$ neutron shell the ground state is observed to be near spherical (in ^{185}Bi it is not sure whether the $1/2^+$ state is the ground state). The decay properties of spherical proton emitters can be understood very well using various theoretical models as shown in ref. [27]. In deformed nuclei, below the closed $N = 82$ neutron shell, the very sensitive proton decay can be used to estimate the degree of nuclear deformation [28,29]. Among the astatine isotopes, the proton separation energies estimated by extrapolating the masses tabulated by Audi *et al.* in ref. [30] indicate that ^{191}At is a good candidate for the observation of proton emission. A rough estimate gives a proton separation energy of approximately -1200 keV for the ^{191}At ground state. This value starts to be negative enough that proton emission would compete successfully with the alpha-particle emission common in this region of the nuclear chart. In addition, a suitable excited state in ^{191}At could be even more favourable for proton decay. However, the masses used for the estimate are based on systematics. By extrapolating the recently measured atomic masses given by Novikov *et al.* in ref. [31], a proton separation energy of approximately -700 keV can be derived. This value is obviously less favourable for the observation of proton emission. All in all, searching for proton emitters above bismuth will be a very interesting task. These nuclei are predicted to have a deformed ground state and will thus offer a challenging test for the theoretical models of proton emission.

The previous studies of ^{193}At were presented in refs. [32,33]. However, the complicated level structure of ^{193}At could not be resolved in a satisfactory manner due to the low statistics obtained for this nucleus.

2 Experimental method

In the present work, the ^{193}At and ^{191}At isotopes were produced in the 4n-evaporation channels of the complete fusion reactions of ^{56}Fe and ^{54}Fe ions with a ^{141}Pr target, respectively. The ion beams were produced by using the volatile-compounds (MIVOC) method [34] in the ECR ion source and were delivered to the target by

the $K = 130$ MeV cyclotron of the Accelerator Laboratory at the Department of Physics of the University of Jyväskylä (JYFL). The average intensities for the $^{56}Fe^{11+}$ and $^{54}Fe^{11+}$ ion beams were 70 pnA and 100 pnA, respectively, measured in a Faraday cup in front of the target. The total-beam-on-target times for ^{56}Fe and ^{54}Fe beams were 56 h and 166 h, respectively.

The excitation function for the production rate of ^{193}At was measured at four bombarding energies, varying from 264 to 272 MeV in the middle of the target. Eight bombarding energies, varying from 248 to 266 MeV in the middle of the target, were used in the determination of the optimum bombarding energy for ^{191}At. The rolled 750 μg/cm^2 ^{141}Pr target was placed between two 40 μg/cm^2 carbon foils and rotated in the ion beam such that the rotating axis was approximately 10 mm off from the primary-beam axis. The fine adjustment of the bombarding energies was performed with a set of thin carbon foils in front of the target. Energy losses in the degrader foils, in the target and also in the helium filling gas (see below) were calculated using the SRIM2000 code [35].

Fusion-evaporation residues were separated in-flight from primary-beam particles and other reaction products using the JYFL gas-filled recoil separator RITU [36]. Separated residues were focused and implanted into a position-sensitive silicon detector at the focal plane of the separator. Before implantation the residues passed through two multiwire proportional avalanche counters, placed 330 mm and 20 mm in front of the silicon detector, providing energy loss and time-of-flight signals. Two 60×60 mm^2 450 μm thick quadrant silicon detectors were placed approximately 5 mm behind the position-sensitive silicon detector. The position-sensitive silicon detector, of thickness 305 μm and of area 80×35 mm^2, was horizontally divided into 16, 5 mm wide position-sensitive strips. The vertical position resolution was better than 500 μm in each strip.

The energy loss signals of the gas counters were used to separate the alpha-particle decays in the silicon detector from the implantations of scattered beam particles and evaporation residues. The time-of-flight between the gas counters combined with the implantation energy of the recoil in the silicon detector was used to separate the candidate fusion-evaporation products from scattered beam particles and transfer products. The quadrant silicon detectors behind the position-sensitive silicon detector were used to detect energetic protons and alpha-particles which were able to punch through the position-sensitive silicon detector [37,38].

The pressure of the helium filling gas in RITU was 0.6 mbar. Instead of using a stationary carbon foil to separate the high-vacuum beam line from the gas filling of RITU, a differential pumping system was developed in order to allow the use of the higher beam currents needed. The common gas volume of the gas counters was filled with 3.0 mbar of isobutane and was separated from the separator gas volume and the silicon detectors high vacuum by 120 μg/cm^2 Mylar foils. The silicon detectors were cooled to 253 K using circulating coolant.

Table 1. Data used for alpha-decay energy calibration.

Nucleus	Alpha-decay energy (keV)	Reference
^{191g}Bi	6310(3)	[39]
^{190}Bi	6429(5)	[39]
^{190}Bi	6455(5)	[39]
^{189g}Bi	6670(15)	[40]
^{189m}Bi	7300(15)	[40]
^{194}Po	6842(6)	[41]
^{193g}Po	6949(5)	[41]
^{193m}Po	7004(5)	[41]
^{192}Po	7167(7)	[41]
^{191g}Po	7334(10)	[42]
^{191m}Po	7378(10)	[42]

Implanted evaporation residues were identified using the method of position and time correlation with the subsequent mother and daughter alpha-decay chains in the silicon detector [43,44]. For gamma and X-ray detection at the focal plane a Compton-suppressed Nordball-type germanium detector with 40% relative efficiency was placed adjacent to the silicon detector.

The alpha-decay energies observed in the silicon detector were calibrated using well-known bismuth and polonium alpha-activities produced during the experiments. The alpha-active nuclei and the corresponding alpha-decay energies used for the calibration are shown in table 1. The energy resolution in the alpha-decay energy spectrum from the sum of all 16 strips was measured to be 25 keV for the 7004 keV ^{193m}Po alpha peak.

3 Experimental results

3.1 The alpha-decay of ^{193}At

A part of the alpha-decay energy spectrum from the reaction ^{56}Fe + ^{141}Pr observed in the silicon detector and vetoed with the gas counters and the punch through detectors is shown in fig. 1a. The spectrum is strongly dominated by activities produced in fusion-reaction channels involving the evaporation of charged particles. Figure 1b shows the same data after requiring a position and time correlation with the implanted residues within a search time of 200 ms from the implantation. The requirement effectively suppresses the longer-living bismuth isotopes, while the polonium isotopes, having almost equal half-lives to the search time, are reduced by a factor of approximately two. Figure 1c shows the data with a further requirement that the alpha-decay is followed by another alpha-decay spatially in the correct position within a search time of 5 s and with an alpha-decay energy between 6500 keV and 7800 keV. The polonium activities are now reduced dramatically due to long-living and mostly beta-active daughter nuclei. Actually, the bismuth and polonium activities should have been totally suppressed after the last requirement but the peaks still appear due

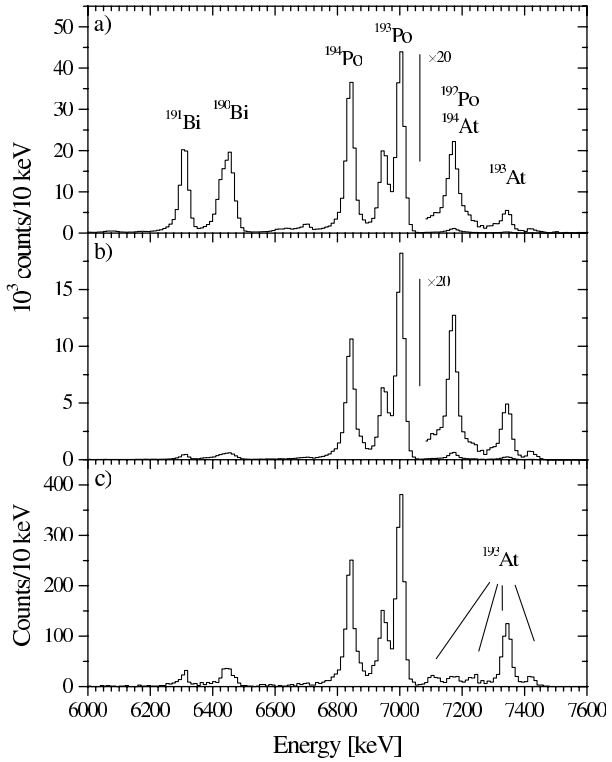

Fig. 1. a) A part of the alpha-decay energy spectrum observed in the silicon detector in the ^{56}Fe + ^{141}Pr measurement. b) The same data after requiring a position and time correlation with the implanted residues within a search time of 200 ms and c) with an additional requirement of subsequent alpha-decay in the same position within 5 s search time and with energy between 6500 keV and 7800 keV.

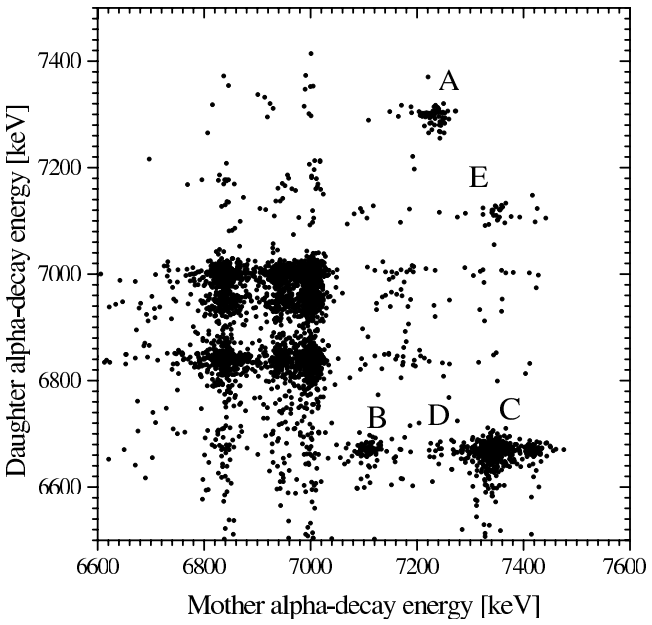

Fig. 2. Two-dimensional plot of the mother and daughter alpha-decay energies for ER–α_m–α_d correlated events observed in the reaction ^{56}Fe + ^{141}Pr. Maximum search times for the ER–α_m and α_m–α_d pairs were 200 ms and 5 s, respectively.

to the accidental correlations with the most intense alpha peaks [43,44].

A two-dimensional mother and daughter alpha-decay energy plot for correlated decay chains of the type evaporation residue–mother alpha-decay–daughter alpha-decay (ER–α_m–α_d) is shown in fig. 2. The alpha-decay correlations from astatine isotopes are clearly visible in the region where the alpha-decay energies of the mother activities are greater than 7000 keV. The area where the mother alpha-decay energies are below 7000 keV is strongly dominated by the accidental correlations from the intense polonium activities. The fairly large number of accidental correlations in fig. 1c and fig. 2 can be understood by taking into account the large number of ER–α_m correlations in fig. 1b. Thus, there are many ER–α_m correlated pairs available for ER–α_m–α_d correlated chains, where the last correlation can be accidental.

Figure 3 shows a two-dimensional energy plot of coincident alpha-decay and gamma-ray events. The gamma-ray events were observed in the focal-plane germanium detector within a 2 μs time interval after the observation of the corresponding alpha-decay energy in the silicon detector. Four groups of previously known alpha-gamma coincidence pairs can be clearly observed and identified. The most intense alpha-gamma coincident pairs with E_α = 6431(4) keV and E_γ = 293.7 keV are associated with the alpha-decay of ^{190m}Bi to an excited state at 293.7 keV in the daughter nucleus ^{186}Tl, decaying by an $E1$ gamma-ray transition to the ground state [45]. The coincident pairs with E_α = 6060(10) keV and E_γ = 185(1) keV were identified as the alpha-decay of ^{192m}Bi to an excited state at 184.6 keV in the ^{188}Tl, decaying by an $E1$ gamma-ray transition to the ground state [45,46]. Two groups of alpha-gamma coincidence pairs were observed for ^{193}Po. The groups with E_α = 6370(7) keV and E_γ = 637(1) keV and with E_α = 6415(7) keV and E_γ = 548(1) keV were identified as the alpha-decays of ^{193m}Po and ^{193g}Po, respectively, to the corresponding excited states in ^{189}Pb [47]. Two clear groups of alpha-gamma coincidences were observed when the alpha-decay energies were greater than 7000 keV. These coincidences are discussed below.

3.1.1 Alpha-decay of the $1/2^+$ state in ^{193}At

The daughter activity of group A in fig. 2 was assigned to originate from the $1/2^+$ isomeric state in ^{189}Bi. The alpha-decay energy E_α = 7295(5) keV and half-life $T_{1/2}$ = $(4.6^{+0.8}_{-0.6})$ ms, determined from 55 ER–α_m–α_d correlated decay chains, are in good agreement with the decay properties of E_α = 7292(6) keV and $T_{1/2}$ = 5.2(6) ms reported for the alpha-decay of the $1/2^+$ state in ^{189}Bi [48]. The corresponding mother activity with the alpha-decay energy E_α = 7235(5) keV and half-life $T_{1/2} = (28^{+5}_{-4})$ ms was assigned to originate from the equivalent $1/2^+$ state in ^{193}At due to the unhindered alpha-decay with a hindrance factor of 0.69(13) determined according to the method of Rasmussen [49] and normalised to the alpha-decay of ^{212}Po.

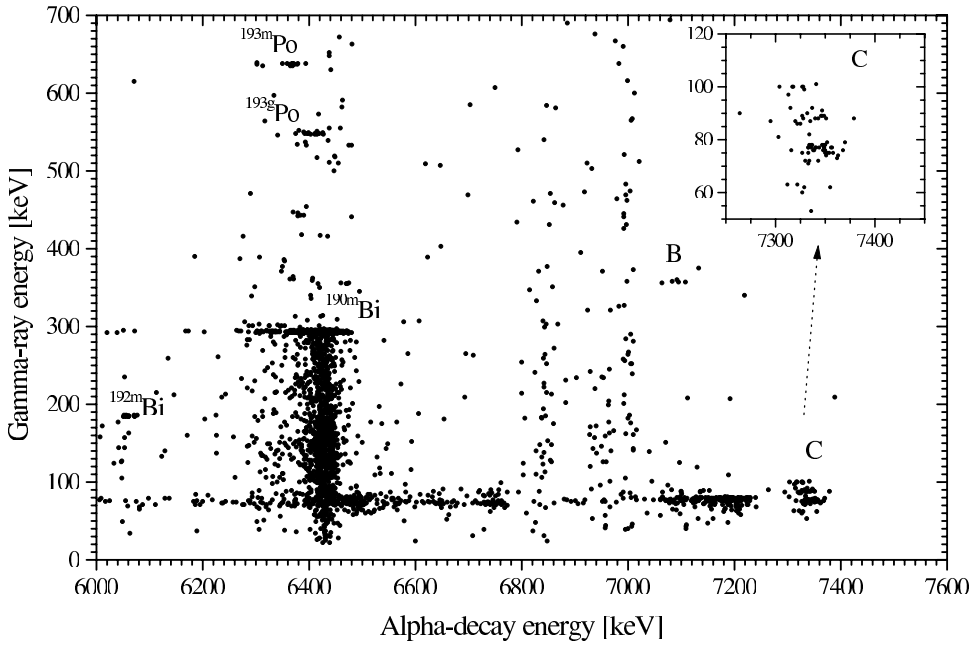

Fig. 3. A two-dimensional plot of the gamma-ray energies observed in the focal-plane germanium detector within a 2 μs time interval after the observation of the corresponding alpha-decay energy in the silicon detector in the ^{56}Fe + ^{141}Pr experiment.

Table 2. The numbers of ER–α_m–α_d correlated decay chains ($N_{obs.}$) observed in different groups in fig. 2. The maximum search times used for ER–α_m and α_m–α_d correlation pairs were 0.2 s and 5 s, respectively. N_{acc}^{triple} represents the expected number of accidentally correlated triple chains, where both ER–α_m and α_m–α_d correlations are random. $N_{acc}^{ER\alpha_m-\alpha_d}$ represents the expected number of accidental correlations between the observed ER–α_m correlations and candidate daughter alpha-decays. The reliability of the estimation, calculated according to ref. [43], was verified by estimating the numbers of $N_{acc}^{ER\alpha_m-\alpha_d}$ correlated chains on the energy region between groups B and E and on the upper left quarter of fig. 2. ER–α_m–α_d correlated decay chains were not expected to appear in these regions.

Group	$N_{obs.}$	N_{acc}^{triple}	$N_{acc}^{ER\alpha_m-\alpha_d}$
A	55	0.005	0.11
B	69	0.06	1.5
C	549	0.04	2.3
D	11	0.04	0.9
E	39	0.04	1.4

The number of correlated triple chains of the type ER–α_m–α_d produced by random correlations in the region of group A in fig. 2 was estimated to be 0.005. Correspondingly, the number of random correlations between the found ER–α_m correlated pairs and the candidate daughter alpha-decays was estimated to be 0.11. The estimations of random correlations, presented also in table 2, were determined according to ref. [43].

3.1.2 Alpha-decay of the $13/2^+$ state in ^{193}At

The interpretation of groups B, C and D in fig. 2 is more complicated. The similarity in the properties of the corresponding daughter activities (E_α = 6668(4) keV and $T_{1/2} = (700^{+100}_{-80})$ ms for group B, E_α = 6666(2) keV and $T_{1/2}$ = 560(25) ms for group C and E_α = 6668(8) keV and $T_{1/2} = (560^{+240}_{-130})$ ms for group D) leads to the conclusion that all these daughter activities originated from the decay of the same initial state. The alpha-decay properties of the daughter activity with E_α = 6667(4) keV and $T_{1/2}$ = 580(25) ms determined from the combined data of groups B, C, and D are broadly compatible with the previously measured results E_α = 6672(5) keV and $T_{1/2}$ = 680(30) ms for the alpha-decay of the $9/2^-$ ground state in ^{189}Bi [46]. The alpha-decay energy spectrum of the corresponding mother activities is shown in fig. 4a as the solid line.

The mother alpha-decay energy E_α = 7106(5) keV and half-life $T_{1/2} = (27^{+4}_{-3})$ ms were determined from the 69 ER–α_m–α_d correlated decay chains of group B in fig. 2. Four of the mother alpha-particles in the decay chains were observed in coincidence with a gamma-ray event in the germanium detector with E_γ = 357.6(5) keV and half-life $T_{1/2} \sim$ 550 ns. Without the requirement of the subsequent daughter alpha-decay one more corresponding ER–α_m–γ correlated coincidence was found. All five alpha-gamma coincidences are clearly observed in fig. 3 marked by B. The properties of the gamma-ray transition are in good agreement with the previously measured properties of an $M2$ transition from the isomeric $13/2^+$ state to the $9/2^-$ ground state in ^{189}Bi with a gamma-ray energy E_γ = 357 keV and half-life $T_{1/2}$ = 880(50) ns [50,51]. The observation of the coincident gamma-ray transition

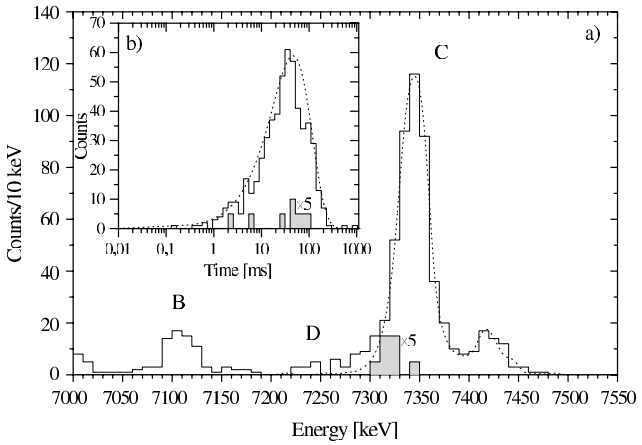

Fig. 4. a) The solid line represents mother alpha-decay energy spectrum in ER–$\alpha_{\rm m}$–$\alpha_{\rm d}$ correlated decay chains where the decay of the $9/2^-$ ground state in ^{189}Bi was observed as a daughter alpha-decay. The dotted line represents the result of a Monte Carlo simulation of the summing-up of the alpha-decay and conversion electron energies in the silicon detector. The filled area (count scale multiplied by a factor of five) shows the energy spectrum of the alpha-decays observed in prompt coincidence with the $E_\gamma = 99.6(5)$ keV gamma-ray events. b) The solid line shows the time distribution of the mother alpha-decays in the ER–$\alpha_{\rm m}$–$\alpha_{\rm d}$ correlated decay chains of group C. The dotted line represents the time distribution of events in a radioactive decay [44] with $T_{1/2} = 31.8$ ms. The filled area (count scale multiplied by a factor of five) shows the time distribution for the ER–$\alpha_{\rm m}$ correlated mother alpha-decays observed in prompt coincidence with the $E_\gamma = 99.6(5)$ keV gamma-ray events.

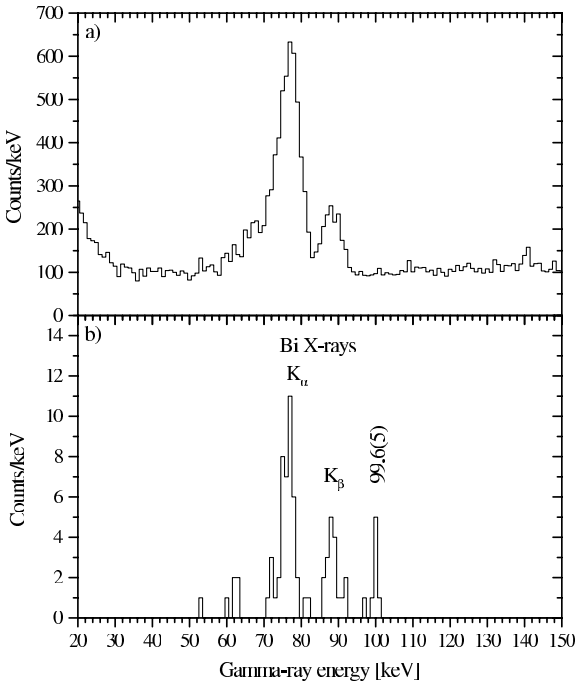

Fig. 5. a) A part of the energy spectrum for gamma-ray events observed in coincidence with any event within a 8 μs time interval in the silicon detector. b) Gamma-ray energy spectrum of group C in fig. 3.

indicates that the alpha-decay of the mother nucleus feeds the $13/2^+$ state in ^{189}Bi. It was concluded that the alpha-decay originates from an equivalent $13/2^+$ state in ^{193}At based on an unexpectedly low hindrance factor ~ 0.24 of the alpha-decay to the $13/2^+$ state when a 100% absolute alpha-decay branching ratio is assumed. The reason for the uncommonly low value of the hindrance factor is discussed in sect. 3.1.4.

Estimates for the numbers of the correlated decay chains produced by the random correlations in the energy region of group B in fig. 2 are presented in table 2.

3.1.3 Alpha-decay of the $7/2^-$ state in ^{193}At

The structure in the mother alpha-decay energy spectrum of group C in fig. 4a (solid line) can be simply explained by fine structure in the alpha-decay corresponding to 88% and 12% branching ratios for the 7345 keV and 7420 keV alpha-decays, respectively. Also the similar half-lives of the peaks lend further support to this hypothesis (see the time distribution of the mother alpha-decays in fig. 4b). Without any additional information this could be the final conclusion. However, by considering the observed gamma-ray events in the germanium detector it was noticed that the structure in the alpha-decay energy spectrum can be better explained by the effect of summing of conversion electron energies with the alpha-decay energies (pile-up of the energy signals in the silicon detector). Similar summing effects were also observed in the alpha-decay of ^{195}At [24].

Figure 5a shows the low-energy part of the gamma-ray energy spectrum observed within 8 μs of any event in the silicon detector. Figure 5b shows the gamma-ray energy spectrum for the alpha-gamma coincidences of group C in fig. 3. In total eight gamma-ray events with an energy $E_\gamma = 99.6(5)$ keV were observed in prompt coincidence ($T_{1/2} < 10$ ns) with alpha-particles. All of the coincident alpha-particles with $E_\alpha = 7322(10)$ keV were correlated with evaporation residues giving a half-life $T_{1/2} = (34^{+19}_{-9})$ ms. The energy spectrum and time distribution of the corresponding mother alpha-decays are presented in fig. 4a and b as the filled spectra. In addition, five of the correlated coincidences were correlated with subsequent daughter alpha-decays with $E_\alpha = 6650(12)$ keV and $T_{1/2} = (310^{+250}_{-100})$ ms. The other two peaks in fig. 5b correspond to the K X-rays of bismuth originating from the internal K conversion of the 99.6(5) keV transition. When taking into account all of the 36 ER–$\alpha_{\rm m}$–$\alpha_{\rm d}$ correlated decay chains where the mother alpha-decay was observed in coincidence with the $E_\gamma = 99.6(5)$ keV gamma-ray or with the corresponding bismuth K X-ray, an alpha-decay energy $E_\alpha = 6662(5)$ keV and half-life $T_{1/2} = (690^{+140}_{-100})$ ms were obtained for the daughter activity.

The observed gamma-ray energy $E_\gamma = 99.6(5)$ keV and half-life $T_{1/2} < 10$ ns limit the possible multipolarity of the transition to $E1$, $M1$ or $E2$. The Weisskopf estimates for the transition corrected for internal conversion

taken from ref. [52] are: $T_{1/2}(E1) = 0.1$ ps, $T_{1/2}(M1) = 2$ ps, $T_{1/2}(E2) = 0.1$ μs and $T_{1/2}(M2) = 1$ μs.

The internal K conversion coefficient was determined from the ratio between the gamma-ray and K X-ray events after corrections for the gamma-ray detector efficiency. The value obtained $\alpha_K = 8.7(20)$ is in good agreement only with the value of $\alpha_K = 8.9$ for an $M1$ transition taken from ref. [52]. The K conversion coefficients of the electric transitions are at least an order of magnitude too low and the coefficients of the other magnetic transitions are approximately one order of magnitude too large.

The energy of the alpha-decay to the 99.6(5) keV excited state in ^{189}Bi was determined from eight alpha-particles in coincidence with the gamma-ray events. The energy spectrum of these alpha-decays is shown in fig. 4a as the filled area. The coincidences with the full-energy gamma-ray events ensures that no additional energy from electron conversion or subsequent X-ray cascade were summed to the alpha-decay energy. The alpha-decay energy to the ground state was determined from the alpha peak above 7400 keV in fig. 4a. The peak represents both the energy of the direct alpha-decay to the ground state and the alpha-decay to the excited state fully summed with the energy emitted in the conversion electron and X-ray cascade. The final values $E_\alpha = 7325(5)$ keV for the alpha-decay energy to the excited state and $E_\alpha = 7423(5)$ keV to the ground state were obtained by taking into account the 99.6(5) keV excitation energy between the final states in ^{189}Bi. The corresponding half-life $T_{1/2} = (31.8^{+1.5}_{-1.3})$ ms of the mother activity was determined from the 549 ER–$\alpha_{\rm m}$–$\alpha_{\rm d}$ correlated decay chains of group C in fig. 2. The half-life is discussed further in sect. 3.1.6 and fig. 6.

A Monte Carlo simulation program [53] was used to study the summing process of the conversion electron energies with the alpha-decay energies in the silicon detector. In the simulation, realistic physical parameters were taken into account. These include, for example, the implantation depth distribution of the evaporation residues in the silicon detector and the energy resolution of the detector. In addition, the energy difference between the ground state and excited state in the daughter nucleus, the alpha-decay energies and branching ratios to these states, the conversion electron energies from different atomic shells and probabilities and ratios of various X-ray yields after electron conversion were considered. The K, L and M conversion coefficients needed for the program were taken from ref. [46].

The dotted line in fig. 4a shows the simulated alpha-decay energy spectrum. In the simulation 98% and 2% alpha-decay branching ratios to the 99.6(5) keV excited state and to the ground state were assumed, respectively. The alpha-decay branching ratios were deduced using the simulation program. An $M1$ character was assumed for the 99.6(5) keV transition in the daughter nucleus. The simulated spectrum is in excellent agreement with the measured spectrum plotted by the solid line in fig. 4a. If any other multipolarity than $M1$ between the states or different alpha-decay branching ratios were assumed in the simulation, no satisfactory correspondence with the measured decay spectrum was reached.

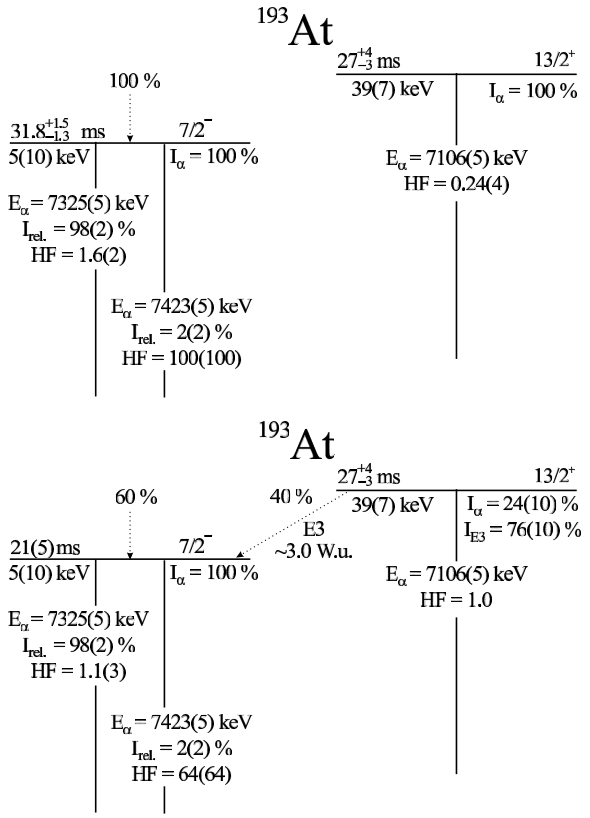

Fig. 6. The decay of the $13/2^+$ state in ^{193}At. In the upper scheme are shown the results observed directly in the measurement. The $7/2^-$ state was assumed to be fed only by the prompt transitions following the neutron evaporation process. The absolute alpha-decay branching ratio from the $13/2^+$ state is assumed to be 100%. In the lower scheme an $E3$ transition between the $13/2^+$ and $7/2^-$ states is assumed. The branching ratios of the alpha-decay and $E3$ transition were estimated by setting the alpha-decay hindrance factor of the $13/2^+$ state to 1.0. It was found that as much as 40% of the feeding of the $7/2^-$ state in ^{193}At would go through the $13/2^+$ state. In the lower scheme, the effect of the long half-life of the feeding state is taken into account in the half-life of the $7/2^-$ state.

After the simulation studies the structure in the mother alpha-decay energy spectrum is well understood. The 7345 keV alpha peak in fig. 4a represents the alpha-decay of ^{193}At to the 99.6(5) keV excited state in ^{189}Bi. A shift of approximately 20 keV compared to the determined alpha-decay energy can be explained by the summing of K conversion electron kinetic energy or the following low-energy (lower than 20 keV, mainly L and M X-rays) X-ray cascade with the alpha-decay energy. According to the simulation, over 90% of the counts in the peak above 7400 keV in fig. 4a originate from the summing process of the alpha-decay energy to the $7/2^-$ state in ^{189}Bi with the energies of the following conversion electron and X-ray cascades. This is estimated from the assumption of a 98% relative branching ratio of the alpha-decay to the excited state used in the simulation.

Based on the half-life, the K conversion coefficient and the result of the simulation, it was concluded that the gamma-ray transition from the 99.6(5) keV excited state to the $9/2^-$ ground state in ^{189}Bi is an $M1$ transition. Thus, the character of the excited state has to be $7/2^-$, $9/2^-$ or $11/2^-$. The assignments of $9/2^-$ and $11/2^-$ can be excluded because only an $M2$ transition with $E_\gamma = 357.6(5)$ keV has been observed from the $13/2^+$ state to the $9/2^-$ ground state in ^{189}Bi [50,51]. If the spin value of the 99.6(5) keV excited state had been 9/2 or higher, at least a weak $M2$ or faster transition with a gamma-ray energy of $E_\gamma \sim 257$ keV should have been observed from the $13/2^+$ state to the excited state. Therefore, the only possible spin and parity assignment of the state at 99.6(5) keV in ^{189}Bi is $7/2^-$.

The unhindered alpha-decay to the $7/2^-$ state in ^{189}Bi indicates that the decay originates from an equivalent $7/2^-$ state in ^{193}At. The corresponding hindrance factor ~ 1.6, when a 98% relative branching ratio to the excited state was assumed, is discussed in sect. 3.1.6.

Estimations for the numbers of the correlated decay chains produced by random correlations are presented in table 2.

3.1.4 Decay of the $1/2^+$ state in ^{189}Bi

An alpha-decay energy $E_\alpha = 7236(9)$ keV and half-life $T_{1/2} = (25^{+11}_{-6})$ ms were determined for the mother activity of group D in fig. 2. The decay properties are similar to those of the mother activity of group A in fig. 2 between the $1/2^+$ states in ^{193}At and ^{189}Bi. However, as mentioned earlier in sect 3.1.2, the subsequent daughter alpha-decay was determined to correspond to the alpha-decay of the $9/2^-$ state in ^{189}Bi. The unobserved link between the $1/2^+$ and $9/2^-$ states in ^{189}Bi could be explained by an $E3$ transition from the $1/2^+$ state to the observed $7/2^-$ state at 99.6(5) keV followed by the $M1$ transition to the $9/2^-$ ground state.

Branching ratios of 83(5)% for the alpha-decay and 17(5)% for the $E3$ gamma-ray transition from the $1/2^+$ state were estimated from the numbers of ER–α_m–α_d correlated decay chains in groups A and D in fig. 2. The corresponding partial half-lives were approximately 5.5 ms and 27 ms for the alpha-decay and $E3$ transition, respectively.

The $1/2^+$ state was observed to be located 187(9) keV above the $9/2^-$ ground state in ^{189}Bi, based on the measured alpha-decay energies of the present work and the previously measured 454 keV excitation energy of the $9/2^-$ state in ^{185}Tl [46] (see sect. 3.1.6). Thus, the energy of the $E3$ transition from the $1/2^+$ state to the $7/2^-$ state in ^{189}Bi would be 87(9) keV. The Weisskopf estimate for an 87 keV $E3$ transition in bismuth isotopes corrected for internal conversion is approximately $T_{1/2}(E3) = 37$ ms. Thus, the strength of the $E3$ transition from the $1/2^+$ state to the $7/2^-$ state in ^{189}Bi would be approximately 1.4 W.u.

3.1.5 Alpha-decay of the $9/2^-$ state in ^{189}Bi

The groups marked by E in fig. 2 originate from the same mother alpha-decay as groups B, C and D, but in this case, the daughter alpha-decay leads directly to the $1/2^+$ ground state in ^{185}Tl. The observed daughter alpha-decay energy of $E_\alpha = 7114(6)$ keV and relative branching ratio 6(3)% are comparable with the results $E_\alpha = 7114(15)$ keV and 3.1(7)% reported in ref. [48].

The absolute alpha-decay branching ratio of the $9/2^-$ ground state in the daughter nucleus ^{189}Bi was determined to be (95–100)%. In the estimation, the numbers of feeding ER–α_m and following ER–α_m–α_d correlated decay chains where the mother alpha-decay is observed in coincidence with the $E_\gamma = 99.6(5)$ keV gamma-ray or with bismuth K X-ray, were used. The requirement of coincidences ensures that especially the ER–α_m correlations originated from the alpha-decay of ^{193}At. Also, a probability of 55% that the alpha-particle deposits all its kinetic energy in the silicon detector and the measured 94(3)% relative alpha-decay branching ratio of the $9/2^-$ ground state in ^{189}Bi to the $9/2^-$ state in ^{185}Tl were taken into account.

3.1.6 Interpretation of the ^{193}At alpha-decay

The alpha-decay energies of the $9/2^-$ ground state in ^{189}Bi to the $9/2^-$ state with $E_\alpha = 6667(4)$ keV and $E_\alpha = 7114(6)$ keV to the $1/2^+$ ground state in ^{185}Tl, were used to verify the excitation energy of the $9/2^-$ state in ^{185}Tl. The obtained value of 457(8) keV is in good agreement with the excitation energy of 454 keV given in ref. [46]. Using an excitation energy of 454 keV for the $9/2^-$ state in ^{185}Tl and the alpha-decay properties of ^{189}Bi observed in the present work, an excitation energy of 187(9) keV was obtained for the $1/2^+$ state in ^{189}Bi. The value is in good agreement with the result 182(8) keV reported in ref. [48].

Based on the alpha-decay properties of ^{193}At and the 187(9) keV excitation energy of the $1/2^+$ state in ^{189}Bi measured in the present work, the $1/2^+$ state was determined to be the ground state in ^{193}At. The $7/2^-$ and $13/2^+$ excited states were discovered to be situated 5(10) keV and 39(7) keV above the ground state, respectively. The excitation energy difference of approximately 34 keV between the $7/2^-$ and $13/2^+$ states, along with the fairly long half-life ($T_{1/2} = (27^{+4}_{-3})$ ms) of the $13/2^+$ state, lead to the possibility of an $E3$ transition from the $13/2^+$ state to the $7/2^-$ state in ^{193}At. The Weisskopf estimate for a 34 keV $E3$ transition corrected for internal conversion taken from ref. [52] is $T_{1/2}(E3) = 107$ ms. The unexpectedly low hindrance factor ~ 0.24 of the alpha-decay of the $13/2^+$ state with $E_\alpha = 7106(5)$ keV also supports the assumption of an additional decay branch from the $13/2^+$ state.

Because the direct observation of the inferred $E3$ transition from the $13/2^+$ state to the $7/2^-$ state was not possible in the present work, the following estimate was made to illustrate the situation. If a common unhindered alpha-decay with $\Delta\ell = 0$ is assumed, the hindrance factor

of the alpha-decay should be about unity. If a hindrance factor equal to unity is assumed for the $E_\alpha = 7106(5)$ keV alpha-decay in ^{193}At the partial half-life of the alpha-decay is 112 ms. The 112 ms partial half-life from the 27 ms half-life gives approximately 24% branching ratio for the alpha-decay. The 76% branching ratio corresponds to a 36 ms partial half-life for the other branches. If it is supposed that the only other significant decay branch from the $13/2^+$ state is an $E3$ transition, it would be approximately 3.0 times faster than the Weisskopf estimate given above.

The assumption of a branching ratio of 76% for the $E3$ transition from the $13/2^+$ state to the $7/2^-$ state in ^{193}At would indicate that 40% of the feeding of the $7/2^-$ state proceeds through the $13/2^+$ state. The feeding $13/2^+$ state with a half-life almost equal to the initial $7/2^-$ state affects the observed half-life of the initial state. When 40% feeding through the $13/2^+$ state with 27 ms half-life was taken into account in the measured 31.8 ms half-life a corrected value of 21 ms was obtained for the half-life of the $7/2^-$ state. These two different feeding paths of the $7/2^-$ state could generate a two-component structure to the decay time distribution presented in fig. 4b. However, any structure or even clear widening was not observed in the distribution. This is actually expected, because normally even a factor of two difference in the half-lives is not enough to be seen in the decay time distribution at this level of statistics. The corrected half-life gives hindrance factors of 1.1(3) and 64(64) for the $E_\alpha = 7325(5)$ keV and the $E_\alpha = 7423(5)$ keV alpha-decay branches from the $7/2^-$ state, respectively. The effect of the possible $E3$ transition from the $13/2^+$ state to the $7/2^-$ state in ^{193}At is illustrated in fig. 6.

Since the energy difference between the lowest-lying $1/2^+$ and $7/2^-$ levels in ^{193}At is only 5(10) keV and the measured half-lives of the states are also almost equal, one may consider if there is just one state which decays with three alpha-decay branches. This assumption would correspond to alpha-decay branching ratios of approximately 2(2)% for the $E_\alpha = 7235(5)$ keV, 89(2)% for the $E_\alpha = 7325(5)$ keV and 9(2)% for the $E_\alpha = 7423(5)$ keV alpha-decay to the $1/2^+$, $7/2^-$ and $9/2^-$ states in the ^{189}Bi daughter nucleus, respectively. By assuming a half-life of 21 ms for the state (discussion would be the same with a half-life of 28 ms) and $\Delta\ell = 0$ for the alpha-decays in ^{193}At, the hindrance factors of approximately 5.8(15), 1.17(10) and 110(110) were obtained for the alpha-decay branches. The alpha-decay with $E_\alpha = 7325(5)$ keV to the $7/2^-$ state in ^{189}Bi clearly represents an unhindered alpha-decay between states with the same spin and parity assignments. Also the alpha-decay with $E_\alpha = 7235(5)$ keV to the $1/2^+$ state gives a low hindrance factor most likely corresponding to a $\Delta\ell = 0$ transition. If $\Delta\ell \geq 1$ transitions are assumed, hindrance factors of approximately 5 or less are obtained. These values are too small to correspond to typical $\Delta\ell \geq 1$ transitions. The alpha-decay with $E_\alpha = 7423(5)$ keV to the $9/2^-$ state in ^{189}Bi clearly shows a hindered character and can be associated with $\Delta\ell \geq 1$ transitions. If a $\Delta\ell = 2$ transition corresponding to an alpha-decay from the $7/2^-$ state to the $9/2^-$ state is assumed a hindrance factor of 64(64) is obtained. This value is in agreement with a $\Delta\ell = 2$ transition. As a conclusion the alpha-decay branches with $E_\alpha = 7325(5)$ keV and $E_\alpha = 7235(5)$ keV show an unhindered character associated with $\Delta\ell = 0$ transitions. However, these transitions were observed to feed the $1/2^+$ and $9/2^-$ states, respectively in the daughter ^{189}Bi nucleus. Based on the spins and parities of the fed states in the daughter nucleus and the definition of the unhindered alpha-decay, these two alpha-decays cannot originate from the same state in ^{193}At. Therefore, the natural explanation of the properties of the observed alpha-decays is that they originate from two different states in ^{193}At. The alpha-decay with $E_\alpha = 7235(5)$ keV originates from a $1/2^+$ state in ^{193}At feeding the $1/2^+$ state in the daughter ^{189}Bi nucleus via unhindered alpha-decay with hindrance factor of 0.69(13) (see sect. 3.1.1). The alpha-decays with $E_\alpha = 7325(5)$ keV and $E_\alpha = 7423(5)$ keV originate from a $7/2^-$ state in ^{193}At feeding the $7/2^-$ and $9/2^-$ states, respectively in the daughter ^{189}Bi nucleus via unhindered and hindered alpha-decays with hindrance factors of 1.1(3) and 64(64), respectively.

3.1.7 The production cross-section of ^{193}At

The total production cross-section of ^{193}At was determined to be $\sigma \sim 40$ nb at the bombarding energy $E = 266$ MeV in the middle of the target for the reaction ^{56}Fe(^{141}Pr, 4n)^{193}At. The production ratios of various states can be estimated from table 2, where the numbers of ER–$\alpha_{\rm m}$–$\alpha_{\rm d}$ correlated decay chains of various groups in fig. 2 are presented. If the $E3$ transition between the $13/2^+$ and $7/2^-$ states were taken into account in the feeding process, the production ratios of $1/2^+$, $7/2^-$ and $13/2^+$ states would be 10%, 50% and 40%, respectively.

3.2 The alpha-decay of ^{191}At

The alpha-decay energy spectrum from the ^{54}Fe + ^{141}Pr reaction observed in the silicon detector and vetoed with the gas counters and the punch through detectors is shown in fig. 7a. Several activities produced in the evaporation of three or four particles involving one or two charged particles dominate the energy spectrum. In fig. 7b the same data is shown after demanding position and time correlation with the implantation of evaporation residues within a 25 ms time interval. The requirement effectively suppresses the longer-living bismuth activities. Figure 7c shows the data with the additional requirement that the alpha-decay be followed by another alpha-decay spatially in the correct position within a search time of 500 ms and with an alpha-decay energy between 6600 keV and 8000 keV. The polonium and bismuth activities are now totally eliminated due to the long-living and mostly beta-active daughter nuclei.

In fig. 8 is shown a two-dimensional mother and daughter alpha-decay energy plot for ER–$\alpha_{\rm m}$–$\alpha_{\rm d}$ correlated decay chains observed in the ^{54}Fe + ^{141}Pr measurement.

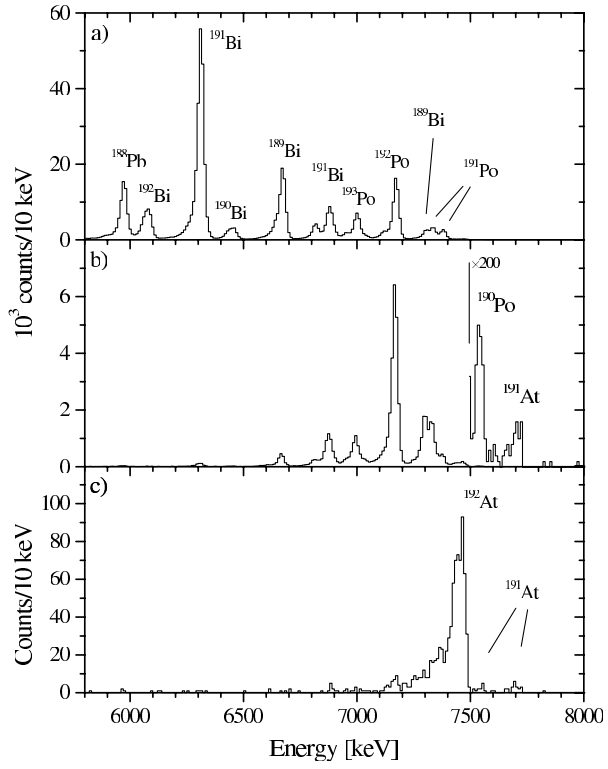

Fig. 7. a) A part of the alpha-decay energy spectrum observed in the silicon detector in the ^{54}Fe + ^{141}Pr measurement. b) The same data after requiring position and time correlation with the implantation of the evaporation residues within a 25 ms time interval and c) with an additional requirement of subsequent alpha-decay in the same position within a 500 ms search time and with alpha-decay energy between 6600 keV and 8000 keV.

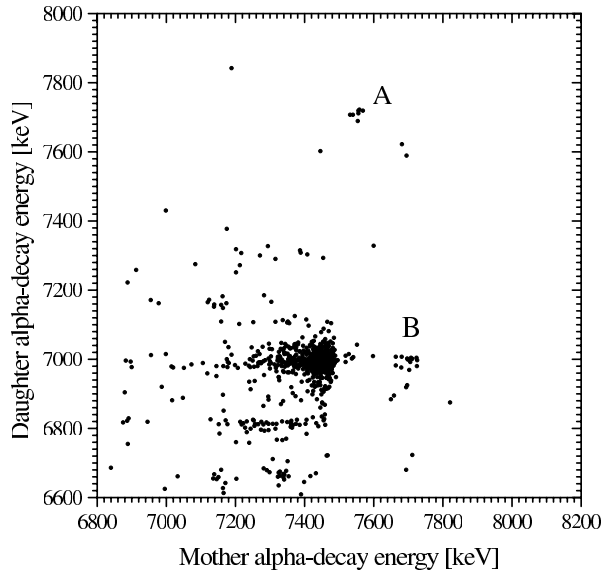

Fig. 8. Two-dimensional display of the mother and daughter alpha-decay energies for ER–α_m–α_d correlated events observed in the reaction ^{54}Fe + ^{141}Pr. Maximum search times for the ER–α_m and α_m–α_d correlated pairs were 25 ms and 500 ms, respectively.

Table 3. The numbers of observed ER–α_m–α_d correlated decay chains ($N_{obs.}$) in different groups in fig. 8. The maximum search times used for ER–α_m and α_m–α_d correlated pairs were 25 ms and 500 ms, respectively. N_{acc}^{triple} represents the expected number of accidentally correlated triple chains, where both correlations ER–α_m and α_m–α_d are random. $N_{acc}^{ER\alpha_m-\alpha_d}$ represents the expected number of accidental correlations between the observed ER–α_m correlations and candidate daughter alpha-decays. The estimates were calculated according to ref. [43].

Group	$N_{obs.}$	N_{acc}^{triple}	$N_{acc}^{ER\alpha_m-\alpha_d}$
A	7	$2 \cdot 10^{-6}$	$3 \cdot 10^{-4}$
B	13	$1 \cdot 10^{-4}$	$6 \cdot 10^{-3}$

Two groups of correlations with mother alpha-decay energy between 7200 keV and 7500 keV and daughter alpha-decay energies approximately 7000 keV and 6800 keV, respectively, were identified as originating from the alpha-decay of a new isotope ^{192}At [54]. The identification of the isotope was based on the observation of the alpha-decay properties of the daughter nucleus in agreement with the alpha-decay properties of ^{188}Bi reported in ref. [45]. Several decay chains originating from ^{193}At can also be identified in fig. 8.

3.2.1 Alpha-decay of the $1/2^+$ state in ^{191}At

The daughter activity of group A in fig. 8 was assigned to originate from the alpha-decay of the $1/2^+$ state in ^{187}Bi. The alpha-decay energy E_α = 7714(11) keV and half-life $T_{1/2} = (310^{+190}_{-90})$ μs were determined from 7 ER–α_m–α_d correlated decay chains. The measured properties are in good agreement with the previously reported values E_α = 7721(15) keV and $T_{1/2} = (290^{+90}_{-50})$ μs for the decay of the $1/2^+$ state in ^{187}Bi [55]. The corresponding mother activity with an alpha-decay energy E_α = 7552(11) keV and half-life $T_{1/2} = (1.7^{+1.1}_{-0.5})$ ms was assigned to originate from the equivalent $1/2^+$ state in ^{191}At due to the unhindered alpha-decay with a hindrance factor of 0.4(3), determined according to ref. [49] (see also table 4 below).

The estimates for the numbers of the correlated decay chains produced by the random correlations in the energy region of the group A in fig. 8 are presented in table 3.

3.2.2 Alpha-decay of the $7/2^-$ state in ^{191}At

The daughter activity of group B in fig. 8 was assigned to originate from the alpha-decay of the $9/2^-$ ground state in ^{187}Bi. The alpha-decay energy E_α = 6994(8) keV and half-life $T_{1/2} = (35^{+14}_{-8})$ ms determined from 13 ER–α_m–α_d correlated decay chains are in good agreement with the previously measured results E_α = 7000(8) keV and $T_{1/2}$ = 32(3) ms reported for the alpha-decay of the $9/2^-$ ground state in ^{187}Bi [55].

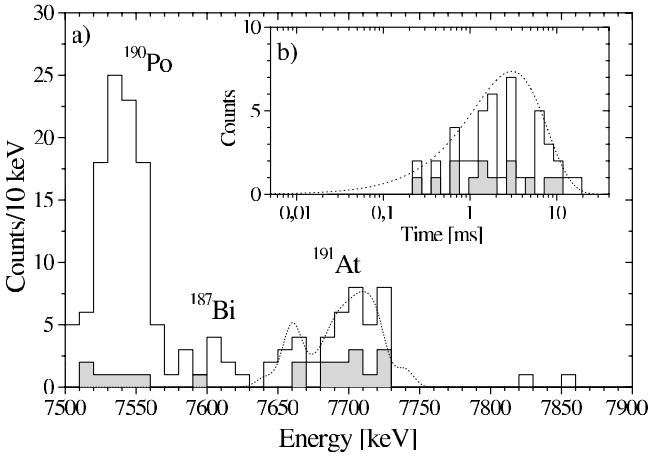

Fig. 9. a) The solid line represents the energy spectrum of ER–α_m correlated alpha-decays (the same as in fig. 7b). The result of the Monte Carlo simulation of summing-up the conversion electron energy with alpha-decay energy in the silicon detector is plotted by the dotted line. The filled area represents the energy spectrum of the ER–α_m–α_d correlated mother alpha-decays followed by a daughter alpha-decay with energy between 6950 keV and 7050 keV (see fig. 8). b) The solid line shows the distribution of the decay times for ER–α_m correlated alpha-particles with decay energy greater than 7640 keV. The filled area shows the same but now for ER–α_m–α_d correlated mother alpha-decays (see fig. 9a). The dotted line represents the density distribution of events in a radioactive decay [44] with $T_{1/2} = 2.1$ ms.

The interpretation of the corresponding mother activity originating from the alpha-decay of ^{191}At is more complicated due to the summing effect of the conversion electron energy with the alpha-decay energy. This phenomenon was discussed in detail in the previous sect. 3.1.3, when the alpha-decay of the $7/2^-$ state in ^{193}At was studied. An expansion of the ER–α_m correlated alpha-decay energy spectrum of fig. 7b is shown in fig. 9a as a solid line. The filled area represents the energy spectrum of mother alpha-decays in ER–α_m–α_d correlated decay chains with daughter alpha-decay energy between 6950 keV and 7050 keV and within a 500 ms time interval after the observation of the mother alpha-decay (see fig. 8).

Two previously known activities are also identified in the ER–α_m correlated alpha-decay energy spectrum in fig. 9a. The ^{190}Po isotope is produced via the p4n-evaporation channel and ^{187}Bi can be produced directly via the α4n-evaporation channel or as an alpha-decay product of ^{191}At. Although the ^{187}Bi events had originated from the alpha-decay of ^{191}At, in the analysis it might look as if they correlate directly with the implantations of the evaporation residues, if the alpha-particles from the decay of ^{191}At escape from the silicon detector.

The possibility that the mother alpha-particle may escape from the silicon detector was taken into account especially when the alpha-decay energy distribution above 7640 keV in fig. 9a was analysed. If the alpha-particle from the decay of the $1/2^+$ state in ^{191}At escapes and the alpha-particle from the daughter decay ($1/2^+$ state in ^{187}Bi) does not escape, one may find an ER–α correlation with $E_\alpha \sim 7714$ keV and $T_{1/2} \sim 2$ ms. To avoid this contamination in ER–α_m correlated decay chains, escaped alpha-particles were also searched for in the analysis. For additional confirmation, the properties of mother alpha-decays in ER–α_m–α_d correlated decay chains with daughter alpha-decay energy in the range 6950–7050 keV are also presented as a filled spectra in figs. 9a and b. The mother alpha-decay energy and decay time distributions in the ER–α_m and ER–α_m–α_d correlated decay chains show the same behaviour.

The width of the ER–α_m correlated alpha-decay energy distribution assigned to ^{191}At in fig. 9a (corresponding to group B in fig. 8) is too large to originate from a single alpha-decay transition. The width of the distribution can be compared to the width of the ^{190}Po alpha-decay peak. The decay scheme of ^{191}At can be based upon that of ^{193}At presented in sect. 3.1.3. Thus, the $7/2^-$ state in ^{191}At alpha-decays to the equivalent excited $7/2^-$ state in ^{187}Bi decaying by an $M1$ transition to the $9/2^-$ ground state. The summing effect of the conversion electron energy with the alpha-decay energy causes the widening in the alpha-decay peak. Contrary to the case of ^{193}At, no gamma-ray events were observed in coincidence with the alpha-decays of ^{191}At mainly due to the poor statistics and low gamma-ray transition energy. Therefore, the excitation energy of the $7/2^-$ state in ^{187}Bi could not be directly measured in the present work. However, the excitation energy can be estimated from the width of the alpha-decay energy distribution. The full width of the structure is approximately 80 keV. When the resolution of the silicon detector is taken into account, it can be estimated that the excitation energy of the $7/2^-$ state in ^{187}Bi would be approximately 60 keV.

As a verification a Monte-Carlo–type program (see sect. 3.1.3) was used to simulate the observed energy spectrum. In the simulation, the $7/2^-$ state in ^{191}At was assumed to alpha-decay to a 63 keV excited $7/2^-$ state in ^{187}Bi, with a 98% relative alpha-decay branching ratio and alpha-decay energy $E_\alpha = 7653$ keV. The 2% relative alpha-decay branching ratio with alpha-decay energy $E_\alpha = 7715$ keV was assumed to lead directly to the $9/2^-$ ground state in ^{187}Bi. The alpha-decay energies and relative branching ratios were estimated using the simulation program. The excited $7/2^-$ state in ^{187}Bi was assumed to decay to the ground state by an $M1$ gamma-ray transition. The L and M conversion coefficients needed for the program were taken from ref. [46].

The result of the simulation is shown in fig. 9a as a dotted line. The simulated spectrum is in good agreement with the measured spectrum. If the use of different alpha-decay energies and branching ratios or any other multipolarity than $M1$ for the transition between the excited state and the ground state in ^{187}Bi were attempted, no satisfactory correspondence between the simulated and the measured spectrum would be reached. The result of the simulation supports the estimation of approximately 60 keV excitation energy of the $7/2^-$ state in ^{187}Bi. The width of the simulated distribution is comparable to the measured

spectrum, and the conversion coefficients, corresponding to a 63 keV $M1$ transition, can create the correct shape of the energy distribution. For gamma-ray energies lower than 80 keV the L conversion coefficient depends strongly on the transition energy. Therefore, even a small change in the estimated excitation energy of the $7/2^-$ state would change the shape of the simulated spectrum dramatically.

A half-life $T_{1/2} = (2.1^{+0.4}_{-0.3})$ ms was determined for the $7/2^-$ state in ^{191}At from 42 ER–α_m correlated decay chains with an alpha-decay energy greater than 7640 keV in fig. 9a. The corresponding time distribution of mother alpha-decays is shown in fig. 9b as solid line. The dotted line represents the density distribution of decay times in a radioactive decay with a half-life of 2.1 ms. The compatibility of the distributions agrees with the assumption that the alpha-decays in the correlated decay chains originate from the same initial state. As an additional confirmation, the time distribution of ER–α_m–α_d correlated mother alpha-decay times of group B in fig. 8 is shown as the filled spectrum in fig. 9b. The corresponding half-life $T_{1/2} = (1.8^{+0.7}_{-0.4})$ ms is comparable with the half-life obtained from the ER–α_m correlated decay chains.

The alpha-decay energies $E_\alpha = 7653(15)$ keV with 98(2)% relative alpha-decay branching ratios to the 63(10) keV excited $7/2^-$ state and $E_\alpha = 7715(15)$ keV with 2(2)% relative branching ratios to the $9/2^-$ ground state in ^{187}Bi, were extracted based on the shape of the alpha-decay spectrum, a result of the simulation and systematics observed in the heavier odd-mass astatine isotopes ^{193}At and ^{195}At [24]. The unhindered alpha-decay to the excited state with a hindrance factor of 1.1(3) supports the interpretation of the similar decay scheme of ^{191}At and ^{193}At.

The $1/2^+$ state was observed to lie 112(20) keV above the $9/2^-$ ground state in ^{187}Bi based on the results measured in the present work and the previously measured 625(17) keV excitation energy of the $9/2^-$ state in ^{183}Tl [55]. The result is in good agreement with the value reported in ref. [55]. Based on this excitation energy of the $1/2^+$ state in ^{187}Bi and the alpha-decay properties deduced for ^{191}At in the present work, the $1/2^+$ state was observed to be the ground state and the $7/2^-$ state 50(30) keV above the ground state in ^{191}At.

Estimates for the numbers of correlated decay chains produced by random correlations in the energy region of group B in fig. 8 are presented in table 3.

3.2.3 Alpha-decay of the $13/2^+$ state in ^{191}At

The possible alpha-decay of the $13/2^+$ state in ^{191}At could be obscured by the correlated alpha-decay chains of ^{192}At in fig. 8 (compare to group B for ^{193}At in fig. 2).

The group with five ER–α_m–α_d correlated decay chains with mother and daughter alpha-decay energies approximately $E_\alpha = 7530$ keV and $E_\alpha = 7000$ keV, respectively most probably originates from the decay of ^{192}At.

An alpha-decay energy $E_\alpha = 7608(16)$ keV and half-life $T_{1/2} = 80^{+120}_{-30}$ ms were obtained for the daughter activity of three decay chains right below group A in fig. 8. Even though the half-life obtained is approximately a factor of two too long, the activity could represent the alpha-decay of the $9/2^-$ state in ^{187}Bi to the $1/2^+$ state in ^{183}Tl, as reported in ref. [55] with $E_\alpha = 7612(15)$ keV and a 8.0% relative alpha-decay branching ratio. Two of the chains with mother alpha-decay energy $E_\alpha = 7688(19)$ keV and half-life $T_{1/2} = 2.6^{+6.0}_{-1.1}$ ms can originate from the decay of the $7/2^-$ state in ^{191}At as discussed above. This would give a 13(8)% relative branching ratio for the alpha-decay of the $9/2^-$ state in ^{187}Bi to the $1/2^+$ state in ^{183}Tl. One chain with a mother alpha-decay energy $E_\alpha = 7446(25)$ keV and decay time of 360 μs (corresponding $T_{1/2} = 250$ μs) could represent the alpha-decay of the $13/2^+$ state in ^{191}At (see fig. 2 for ^{193}At). The alpha-decay energy of the mother activity would support the assumption of the hidden group of ^{191}At decay chains under the decay chains of ^{192}At. An unhindered alpha-decay with decay energy $E_\alpha = 7446$ keV in ^{191}At would represent approximately a 8.8 ms half-life if a hindrance factor equal to unity is assumed. Thus, the observation of one decay with 250 μs half-life is unlikely but nevertheless possible. See also the excitation energy discussion in sect. 4.3.5.

3.2.4 Alpha-decay of the $9/2^-$ state in ^{187}Bi

The absolute alpha-decay branching ratio of the $9/2^-$ ground state in ^{187}Bi can be estimated from the numbers of ER–α_m and ER–α_m–α_d correlated decay chains originating from the alpha-decay of the $7/2^-$ state in ^{191}At (events above 7640 keV in fig. 9a). In the estimation, a probability of 55% that the alpha-particle deposits all its kinetic energy in the silicon detector and a relative alpha-decay branching ratio of 87(8)% (see sect. 3.2.3) for the decay of the $9/2^-$ ground state in ^{187}Bi to the $9/2^-$ state in ^{183}Tl are taken into account. The obtained result of 65(30)% for the absolute alpha-decay branching ratio of the $9/2^-$ ground state in ^{187}Bi is surprisingly low. The branching ratio of the competing beta-decay should be on the order of 2%, if the beta-decay half-life of 2.4 s given in ref. [56] is assumed. Of course, the statistics are very low for the determination of these alpha-decay branching ratios. Also, the ER–α_m correlated decay chains may include a few decay chains where the alpha-decays of the $1/2^+$ state in the daughter nucleus ^{187}Bi are correlated directly with evaporation residues, if the alpha-particle of the mother decay ($1/2^+$ state in ^{191}At) escapes. This possibility was discussed earlier in sect. 3.2.2. Due to these uncertainties, an absolute alpha-decay branching ratio of 100% was used in the analysis.

3.2.5 Production cross-section of ^{191}At

The total production cross-section of ^{191}At was determined to be approximately $\sigma \sim 300$ pb at the bombarding energy $E = 260$ MeV in the middle of the target for the reaction ^{141}Pr(^{54}Fe, 4n)^{191}At.

The production ratios of different states can be estimated from table 3, where the numbers of ER–α_m–α_d

Table 4. The measured alpha-decay properties for ^{191}At and ^{193}At and also for the corresponding daughter nuclei. The literature values and assignments for ^{187}Bi and ^{189}Bi are taken from refs. [55,46,48]. The hindrance factors and reduced widths are calculated from measured values using the method of Rasmussen [49] and normalised to the alpha-decay of ^{212}Po. In the calculation, the $\Delta\ell$ values of the transitions were taken into account.

Nucleus	E_α (keV)		$T_{1/2}$ (ms)		$I_{\mathrm{rel.}}$ (%)		HF	δ^2(keV)	$\Delta\ell$	Assignment
	This work	Lit.	This work	Lit.	This work	Lit.				
^{191g}At	7552(11)		$1.7^{+1.1}_{-0.5}$		100		0.4(3)	150(100)	0	$1/2^+ \rightarrow 1/2^+$
^{191m}At	7653(15)		$2.1^{+0.4}_{-0.3}$		98(2)		1.1(3)	59(13)	0	$7/2^- \rightarrow 7/2^-$
^{191m}At	7715(13)		$2.1^{+0.4}_{-0.3}$		2(2)		50(50)	1.3(13)	2	$7/2^- \rightarrow 9/2^-$
^{193g}At	7235(5)		28^{+5}_{-4}		100		0.69(13)	93(17)	0	$1/2^+ \rightarrow 1/2^+$
^{193m}At	7325(5)		21(5)[a]		98(2)		1.1(3)	60(15)	0	$7/2^- \rightarrow 7/2^-$
^{193m}At	7423(5)		21(5)[a]		2(2)		64(64)	1.0(10)	2	$7/2^- \rightarrow 9/2^-$
^{193m}At[b]	7106(5)		27^{+4}_{-3}		100		1.0(4)	64(30)	0	$13/2^+ \rightarrow 13/2^+$
^{187g}Bi	6994(8)	7000(8)	35^{+14}_{-8}	32(3)	87(8)	88.3	0.8(3)	80(30)	0	$9/2^- \rightarrow 9/2^-$
^{187g}Bi	7605(16)	7612(15)	35^{+14}_{-8}	25^{+9}_{-5}	13(8)	8.0	40(30)	1.7(13)	5	$9/2^- \rightarrow 1/2^+$
^{187g}Bi[c]		7367(30)		21^{+29}_{-8}		3.7				$9/2^- \rightarrow 3/2^+$
^{187m}Bi	7714(11)	7721(15)	$0.31^{+0.19}_{-0.09}$	$0.29^{+0.09}_{-0.05}$	100	100	1.3(8)	52(30)	0	$1/2^+ \rightarrow 1/2^+$
^{189g}Bi	6667(4)	6672(5)	580(25)	680(30)	94(3)	95(2)	0.89(6)	73(5)	0	$9/2^- \rightarrow 9/2^-$
^{189g}Bi	7114(6)	7114(6)	580(25)	~ 1000	6(3)	3.1(7)	40(20)	1.7(9)	5	$9/2^- \rightarrow 1/2^+$
^{189g}Bi[c]		6550(15)		~ 1000		1.2(9)				$(9/2^- \rightarrow 11/2^-)$
^{189g}Bi[c]		6833(7)		1400^{+1000}_{-800}		1.3(6)				$9/2^- \rightarrow 3/2^+$
^{189m}Bi[d]	7295(5)	7292(6)	$4.6^{+0.8}_{-0.6}$	5.2(6)	100	88(3)	1.2(3)	55(10)	0	$1/2^+ \rightarrow 1/2^+$
^{189m}Bi[e]		7114(7)		8(4)		12(3)				

([a]) This is the corrected value (measured value without correction is $(31.8^{+1.5}_{-1.3})$ ms). See text and fig. 6 for more details.
([b]) The absolute alpha-decay branching ratio was estimated to be 24(10)% using hindrance factor. See text and fig. 6 for more details.
([c]) These transitions were not attempted to be identified in the present work (see sect. 4).
([d]) The absolute alpha-decay and $E3$ transition branching ratios were estimated to be 83(5)% and 17(5)%, respectively.
([e]) This transition was not detected in the present work (see sect. 4).

correlated decay chains for different groups in fig. 8 are presented. If the absolute alpha-decay branching ratios of the daughter nucleus ^{187}Bi are assumed to be 100%, the production ratios for $1/2^+$ and $7/2^-$ states in ^{191}At are estimated to be 32% and 68%, respectively.

4 Discussion

The results obtained in the present work are shown in table 4. The decay properties of the daughter nuclei ^{187}Bi and ^{189}Bi are compared with the previous experimental results. The assignments shown for the alpha-decays of ^{187}Bi and ^{189}Bi are taken from refs. [55,48]. Some of the weakest alpha-decay branches reported in refs. [55,48] were not observed. In most of the cases this was due to the low statistics obtained for these nuclei produced via alpha-decay in the present work.

The results obtained for ^{187}Bi are in good agreement with the previous experimental results, though the weakest alpha-decay branch from the $9/2^-$ ground state to the $3/2^+$ state in ^{183}Tl was not observed.

In the case of ^{189}Bi two clear alpha-decay branches were detected from the $9/2^-$ ground state being in agreement with previous results. Two other alpha-decay branches with relative branching ratios of approximately 1.3% [48], could not be detected so clearly. The reported alpha-decay energies 6550(15) keV and 6833(7) keV [48] would appear in the ER–α_{m}–α_{d} correlated events in the region where some accidentally correlated decay chains could also be expected in fig. 2. Therefore, the identification of these weak branches was not attempted. The alpha-decay energy $E_\alpha = 7295(15)$ keV for the decay of the $1/2^+$ state in ^{189}Bi is in good agreement with the result reported in ref. [48]. Another alpha-decay branch with branching ratio of 12(3)% and alpha-decay energy $E_\alpha = 7114(7)$ keV from the $1/2^+$ state reported in ref. [48] was not detected in the present work, although it should have been clearly observed. Instead of the 12(3)% alpha-decay branch, a 17(5)% $E3$ gamma-ray transition branch from the $1/2^+$ state to the $7/2^-$ state in ^{189}Bi was deduced (see fig. 10).

4.1 The decay schemes

The proposed alpha-decay schemes of ^{191}At and ^{193}At with the observed decay properties of the corresponding

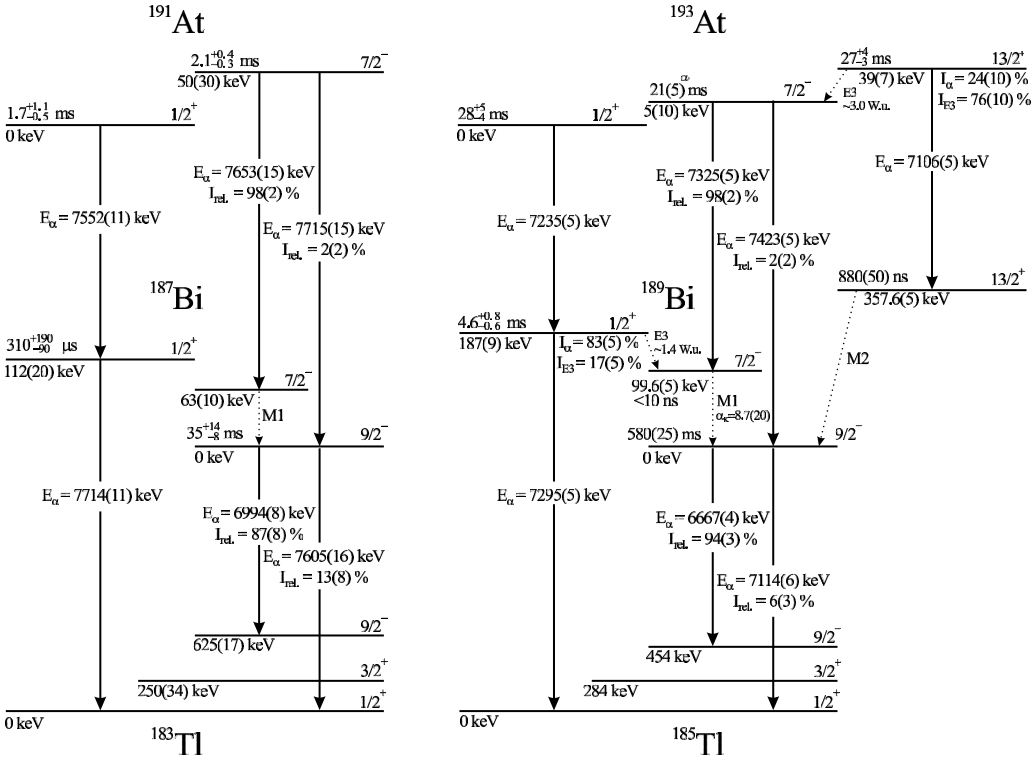

Fig. 10. Proposed alpha-decay schemes of ^{191}At and ^{193}At. The decay properties of the $13/2^+$ state shown for ^{189}Bi were taken from refs. [50,51]. $^{\alpha}$: this is the corrected value (measured value without correction is $(31.8^{+1.5}_{-1.3})$ ms). See text and fig. 6 for more details.

daughter nuclei ^{187}Bi and ^{189}Bi are shown in fig. 10. The observations that led to the presented interpretations are discussed in detail in sects 3.1 and 3.2. The alpha-decay schemes are very similar to the decay scheme of ^{195}At, which was suggested to differ dramatically from the systematics seen in heavier odd-mass astatine isotopes [24]. In ^{195}At the intruder $1/2^+$ state was observed to become the ground state and the first-excited state was suggested to be a $7/2^-$ state. In heavier odd-mass astatine isotopes between ^{197}At and ^{211}At the $9/2^-$ state was seen to be the ground state and a low-lying $7/2^-$ state has not been observed in astatine isotopes between ^{197}At and ^{203}At.

4.2 Mass excess

A mass excess of $-250(110)$ keV is given for ^{193}At by Novikov *et al.* in ref. [31]. This value is derived from the previous results presented for the alpha-decay of ^{193}At in refs. [32,33]. Using the decay properties presented for ^{193}At in fig. 10 and the mass excess of $-10170(110)$ keV given for the daughter nucleus ^{189}Bi in ref. [31], a mass excess of $-170(110)$ keV is obtained for ^{193}At in the present work.

The mass of ^{187}Bi is needed to estimate the mass of ^{191}At. However, there is no measured information about the mass of ^{187}Bi so far. Also, the extrapolated masses for the lightest ($A < 193$) odd-mass bismuth isotopes given by Audi *et al.* [30] differ increasingly with decreasing neutron number from the measured masses given in refs. [31,57]. Therefore, the mass of ^{187}Bi is approximated from the measured results of the closest odd-mass bismuth isotopes. Since the proton binding energy of the $1/2^+$ state in ^{185}Bi is known [25,26] and the corresponding binding energy in the heavier odd-mass bismuth isotopes starting from ^{189}Bi can be calculated using the measured masses [31, 57], the mass of ^{187}Bi is approximated from the behaviour of the $1/2^+$ state in odd-mass bismuth isotopes. A mass excess of $-6450(120)$ keV is estimated for the $9/2^-$ ground state in ^{187}Bi after the approximation. Using the alpha-decay properties presented for ^{191}At in fig. 10 and the mass excess derived for the daughter nucleus ^{187}Bi above, a mass excess of 3800(120) keV is obtained for ^{191}At. It must be noted, however, that a use of the approximation covers and hides interesting and unexpected details within the systematics.

4.3 Systematics

The systematics of low-lying states in light odd-mass astatine isotopes compared to the ground states is shown in fig. 11. Data for isotopes from $A = 195$ to 207 were taken from refs. [24,23,21,58,22,59,46].

The $9/2^-$ state, associated with the $(\pi h_{9/2})^3$ configuration coupled to the 0^+ lead core, was determined to be the ground state in odd-mass astatine isotopes from ^{211}At to ^{197}At. The excitation energy of the isomeric $13/2^+$ state drops increasingly when moving from the closed $N = 126$

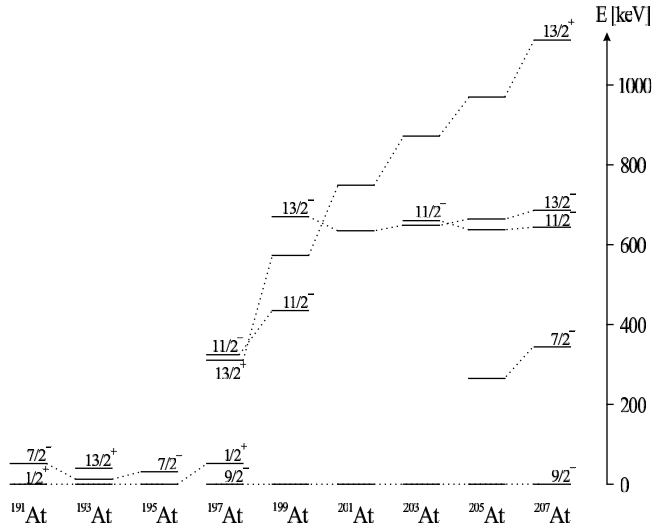

Fig. 11. Systematics of low-lying levels in odd-mass astatine isotopes. The states linked with dotted lines have the same spin and parity assignments.

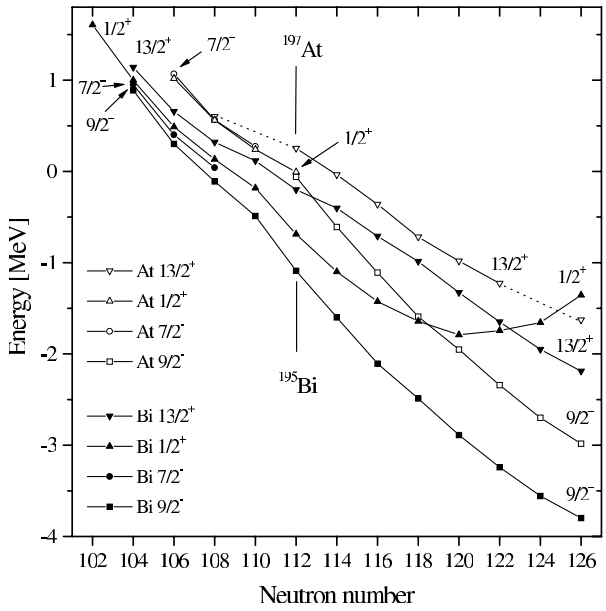

Fig. 12. Proton binding energies of odd-mass bismuth and astatine isotopes. The energies of the excited states were obtained by simply adding the excitation energies to the corresponding binding energy of the ground state.

neutron shell towards the $N = 104$ neutron mid-shell region. Between the ^{197}At and ^{195}At isotopes the ground state changes from the $9/2^-$ state to the intruder $1/2^+$ state. The $9/2^-$ state has not been observed in the light odd-mass ($A < 197$) astatine isotopes so far.

The change in the character of the ground state to which the excitation energy of the other states are compared may be misleading when studying the behaviour of the excited states. For example in ^{193}At the $9/2^-$ state may be located above the $13/2^+$ state, which would mean an even deeper drop of the $13/2^+$ state than that expected from fig. 11.

In order to study the behaviour of the states in light odd-mass astatine isotopes, proton binding energy systematics are constructed and shown for light bismuth and astatine isotopes in fig. 12. The masses needed for the plot were taken from the recent atomic mass measurements [31, 57, 30], updated with the new results for ^{191}At, ^{193}At and ^{187}Bi presented in sect. 4.2. An overall accuracy of approximately 100 keV was given for the measured masses.

The behaviour of excited states was obtained by simply adding the excitation energy to the corresponding binding energy of the ground state in fig. 12. The excitation energies for astatine isotopes from mass number $A = 195$ to 211 were taken from refs. [24, 23, 21, 58, 22, 59, 46] and for bismuth isotopes from refs. [51, 48, 50, 60, 61, 24, 46] and from the present work. The positive binding energies in fig. 12 indicate that the states are not any more proton bound compared to the ground state of the corresponding daughter nucleus.

For a more illustrative view of the systematics, the graphs in fig. 12 are presented again in fig. 13, but now the energies are compared to the $9/2^-$ ground state in bismuth isotopes. This was done to get a better idea about the behaviour of the states in light odd-mass astatine isotopes where they cannot be compared to the $9/2^-$ state as in the heavier odd-mass astatine isotopes starting from ^{197}At.

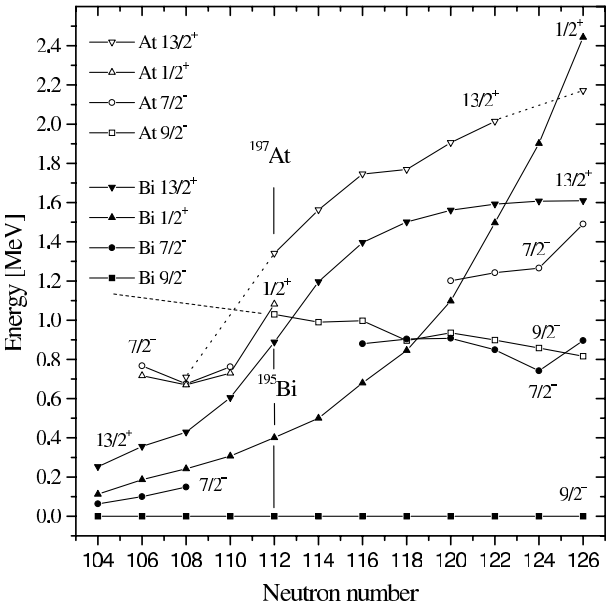

Fig. 13. The same data as in fig. 12 but now normalised to the $9/2^-$ ground state in bismuth. The plot was done to visualise the behaviour of the states in light astatine isotopes where the $9/2^-$ state is not known. See text for more details.

As can be seen in figs. 12 and 13, the proton binding energy of the $9/2^-$ state in astatine isotopes follows smoothly the corresponding binding energy of the $9/2^-$ state in bismuth isotopes. The only differences between the binding energy curves are a shift and a small slope difference. If it is assumed that the $9/2^-$ state in astatine isotopes follows the $9/2^-$ ground state of bismuth isotopes in the same way also in the lightest isotopes (as

an extended dotted line in fig. 13), it would be straightforward to estimate the behaviour of the $1/2^+$, $7/2^-$ and $13/2^+$ states compared to the $9/2^-$ state also in these light astatine isotopes.

4.3.1 The $9/2^-$ states

The $9/2^-$ ground states in bismuth and astatine isotopes are associated with nearly spherical configurations with the last proton occupying the $\pi h_{9/2}$ orbital. As mentioned above, the proton binding energies of the $9/2^-$ states in bismuth and astatine isotopes show similar behaviour up to ^{197}At, until the $1/2^+$ state crosses the $9/2^-$ state in astatine isotopes as shown in fig. 12. The $1/2^+$ state can be associated with a slightly oblate $\pi(4p-1h)$ configuration analogous to the bismuth isotopes. The $7/2^-$ state, also with a slightly oblate deformed configuration (see sect. 4.3.2 and ref. [24]), closely follows the $1/2^+$ state in light astatine and also in light bismuth isotopes. The crossing of the two different configurations in astatine isotopes (in ^{197}At) creates a very clear and understandable bend to the ground-state proton binding energy curve derived using the measured masses from refs. [31,57,30]. It is surprising that a similar bend appears also in the proton binding energy curve of the $9/2^-$ ground state and also in the curves of the $1/2^+$ and $13/2^+$ states shown for bismuth isotopes in fig. 12. If the bend in the astatine isotopes can be interpreted as originating from the change of the nuclear shape from spherical to slightly oblate, the corresponding bend in the bismuth isotopes may indicate a similar change in the nuclear structure. Since the bend of each curve shown for bismuth occurs in the same ^{193}Bi isotope, it may be due to a systematic error in the atomic mass data. However, the bend in the light bismuth and astatine isotopes is hundreds of kiloelectronvolts from the behaviour expected based on the systematics in the heavier isotopes. On the other hand, an overall accuracy of approximately 100 keV was given for the measured masses presented in refs. [31,57,30]. It was also checked that the structures in the proton binding energies are due to the changes in the systematics of bismuth and astatine masses rather than in the respective lead and polonium daughter nuclei.

4.3.2 The $7/2^-$ states

So far, a low-lying $7/2^-$ state has not been observed in neutron-deficient odd-mass astatine isotopes between ^{197}At and ^{203}At. Correspondingly, the $9/2^-$ state has not been observed in the light ($A < 197$) astatine isotopes. As already mentioned in sect. 1, the emergence of the $7/2^-$ state over the $9/2^-$ state can be explained by a change in the deformation of this three-particle configuration between ^{197}At and ^{195}At isotopes. Since no sizeable ground state deformation was observed in ^{197}At [23], the odd proton in the $1h_{9/2}$ orbital creates the $9/2^-$ ground state, associated with the $(\pi h_{9/2})^3$ configuration. According to the Nilsson diagram a $7/2^-$ state, associated with an oblate $7/2^-[514]$ Nilsson state, originating predominantly from the $\pi h_{9/2}$ orbital at sphericity and having a mixed $\pi f_{7/2}/\pi h_{9/2}$ character at oblate deformation, becomes available for the last 85th proton in odd-mass astatine isotopes if sufficient oblate deformation is assumed. Based on the results obtained in the present work and in ref. [24], it is proposed that the deformed three-particle configuration, driving the last proton to the $7/2^-[514]$ Nilsson state, is energetically more favoured than the nearly spherical $(\pi h_{9/2})^3$ configuration in light $A < 197$ odd-mass astatine isotopes. A sudden change in the ground-state deformation from a nearly spherical shape to an oblate shape is theoretically predicted to happen between ^{199}At and ^{198}At by Möller *et al.* in ref. [9].

In relation to astatine isotopes, the existence of a low-lying $7/2^-$ state in bismuth isotopes can be understood by the single-particle $7/2^-[514]$ Nilsson proton state. In fact, the $7/2^-[514]$ state is the only simple possibility to generate a low-lying $7/2^-$ state in bismuth isotopes. The identification of this state in light bismuth isotopes in ref. [24] and the present work is a very good example of the power of the combined alpha-decay and gamma-ray transition measurements to study low-lying non-yrast states in exotic heavy nuclei.

The strength of the deduced $E3$ transition from the $13/2^+$ state can be used to probe the configuration of the final $7/2^-$ state in ^{193}At. The $13/2^+$ state can be thought of as consisting of an admixture of a $\pi i_{13/2}$ orbital coupled to the 0^+ lead core and a $\pi f_{7/2}$ orbital coupled to an octupole excited 3^- lead core [62]. Thus, the $E3$ transition may correspond to orbital transitions of the type $\pi i_{13/2} \rightarrow \pi h_{9/2}$ or $\pi i_{13/2} \rightarrow \pi f_{7/2}$, respectively, where the latter one would be considerably enhanced by the collective $3^- \rightarrow 0^+$ core transition. The similar $E3$ transitions are discussed in refs. [63,64], where the typical $E3$ transition strengths of 3 W.u. and over 20 W.u. were reported for the orbital changes of the type $\pi i_{13/2} \rightarrow \pi h_{9/2}$ and $\pi i_{13/2} \rightarrow \pi f_{7/2}$, respectively, in the trans-lead region. The observed $E3$ transition strength of 3.0 W.u. (highest limit 4.0 W.u.) would be consistent with a $\pi i_{13/2} \rightarrow \pi h_{9/2}$ orbital transition. The value would indicate, that the dominant component of the final $7/2^-$ state would come from the $\pi h_{9/2}$ orbital and that the deformation of the states would not be very strong [64]. On the other hand, it should be noticed that in the $E3$ transition strength systematics shown in refs. [63,64], the transition energies were all above 300 keV, while in the present case the transition energy is only approximately 34 keV. So it is not so clear if the $E3$ transition strengths would behave the same way for lower transition energies than those presented in refs. [63,64].

4.3.3 The $1/2^+$ state in bismuth isotopes

The parabolic behaviour of the $1/2^+$ intruder state is a well-known feature in the odd-mass bismuth isotopes shown in fig. 13. The downward trend of the state compared to the $9/2^-$ ground state is observed to continue up

to ^{187}Bi at the neutron mid-shell ($N = 104$) without any sign of levelling off [55]. In ref. [55] it is speculated that the continuation of the downward trend could originate from a crossing of two different $1/2^+$ states. A weakly oblate deformed intruder $\pi(2p-1h)$ configuration would create the parabolic behaviour in the heavier odd-mass bismuth isotopes. In the lighter isotopes the prolate $1/2^+$ state —a prolate $1/2^+[660]$ Nilsson proton orbital was suggested in ref. [55]— would cross the oblate configuration and continue the downward trend of the $1/2^+$ state. The assumption was based on the coexistence of oblate, prolate and also spherical shapes observed in lead isotopes [4].

The strength of the $E3$ transition from the $1/2^+$ state to the $7/2^-$ state in bismuth (see sect. 3.1.4 and fig. 10) can possibly be used to deduce the properties of the initial and final states. In ^{189}Bi the strength of 1.4 W.u. is deduced for the $E3$ transition as mentioned in sect. 3.1.4, but in ^{191}Bi a strength of only 0.09 W.u. was obtained [24]. The latter value represents a typical single-particle $E3$ transition strength in this region of the nuclear chart. The first value indicates that the corresponding transition in ^{189}Bi could include collective components. This sudden increase in the strength of the transition would suggest a change in the configuration of the initial $1/2^+$ state or the final $7/2^-$ state between ^{191}Bi and ^{189}Bi isotopes.

The $1/2^+$ state is associated with the weakly oblate deformed $\pi(2p-1h)$ configuration originating mainly from a proton hole in the $s_{1/2}$ orbital. The $7/2^-$ state can be associated with an oblate $7/2^-[514]$ Nilsson proton state originating predominantly from the $\pi h_{9/2}$ orbital at sphericity and having a mixed $\pi f_{7/2}/\pi h_{9/2}$ character at oblate deformations (see also sect. 4.3.2). Thus, the $E3$ transition between the states would mainly be of the type $\pi s_{1/2} \rightarrow \pi f_{7/2}/\pi h_{9/2}$, depending on the deformation of the final $7/2^-$ state. If the main component of the final state originated from the $\pi h_{9/2}$ orbital, the $E3$ transition could be considered as a normal single-particle orbital change. This would be consistent with the deduced transition strength of 0.09 W.u. reported for ^{191}Bi in ref. [24]. On the other hand, if the main component of the final state originated from the $\pi f_{7/2}$ orbital, the strength of the $E3$ transition could be enhanced. As mentioned earlier, the main component of the $1/2^+$ state probably originates from a single $\pi s_{1/2}$ proton coupled to the 0^+ lead core. One component of the state might originate from the $\pi f_{7/2}$ proton coupled to an octupole excited 3^- lead core [65]. Thus, the initial $1/2^+$ state and the final $7/2^-$ state would consist of a component from the same $\pi f_{7/2}$ orbital coupled with the lead core. The de-excitation of the collective 3^- core would explain the sudden increase in the strength of the $E3$ transition in ^{189}Bi. This explanation would, however, require an unexpected sudden change in the structure of the $7/2^-$ final state between ^{191}Bi and ^{189}Bi. The $h_{9/2}$ and the $f_{7/2}$ orbitals are located so close to each other (especially when Woods-Saxon or Yukawa single-particle levels are used) that the mixing of the orbitals should change very smoothly over a wide range of oblate deformations.

Another explanation for the increased $E3$ transition strength could be the sudden change in the structure of the initial state. If the initial $1/2^+$ state turned into a prolate $1/2^+[660]$ Nilsson proton state in light bismuth isotopes as suggested in ref. [55], it could consist of an admixture of a $\pi i_{13/2}$ orbital coupled to the 0^+ lead core and a $\pi f_{7/2}$ orbital coupled to an octupole excited 3^- lead core. Since the $7/2^-$ final state is $\pi f_{7/2}/\pi h_{9/2}$ of parentage, the initial state may contain a component of the final state coupled to an octupole excited core. Thus, in addition to the single-particle $E3$ transition, de-excitation of the collective core from the 3^- state to the 0^+ state would enhance considerably the strength of the $E3$ transition. This transition would belong to the same category as the enhanced $\pi i_{13/2} \rightarrow \pi f_{7/2}$ transition discussed in sect. 4.3.2.

However, the $1/2^+$ state should not be the lowest member of the states originated from a prolate $1/2^+[660]$ Nilsson proton orbital due to the Coriolis interaction in deformed nuclei. The Coriolis effect is observed to be very large for single-particle orbitals with $K = 1/2$ and high j as in the case of the $1/2^+[660]$ orbital [66]. This would cause among other things that the $13/2^+$ state is one of the lowest (or the lowest) lying levels and the $1/2^+$ level would lie somewhere higher in energy.

Although the strength of the enhanced $E3$ transition in ^{189}Bi is somewhat lower than the values presented in refs. [63,64], the transition is approximately 15 times faster than the corresponding transition in ^{191}Bi. This difference cannot be explained by an uncertainty in the conversion coefficients or something similar because the energies of both transitions are almost exactly 90 keV. A satisfactory explanation for the enhanced (collective) $E3$ transition in ^{189}Bi is difficult to give based on the present data. Further studies like in-beam gamma-ray spectroscopic measurements would give direct knowledge about the structure of the $7/2^-$ and $1/2^+$ states in light odd-mass bismuth isotopes.

4.3.4 The $1/2^+$ state in astatine isotopes

The $1/2^+$ state is observed in light odd-mass astatine isotopes starting from ^{197}At with 52(10) keV excitation energy compared to the $9/2^-$ ground state [58]. In the lighter isotopes the $1/2^+$ state is observed to become the ground state and the $9/2^-$ state is not observed any longer. If the behaviour of the $9/2^-$ state in astatine isotopes is assumed to be smooth, as sketched by the dotted line in fig. 13, the $1/2^+$ state drops deeply, approximately 330 keV, 410 keV and 400 keV below the assumed $9/2^-$ state in ^{195}At, ^{193}At and ^{191}At, respectively. The behaviour of the $1/2^+$ state in the astatine isotopes follows the behaviour of the corresponding $1/2^+$ state in the bismuth isotopes, until it seems to level off in ^{191}At. Of course, it should be remembered that the accuracy of the masses is approximately 100 keV and that the mass of ^{191}At is derived from the approximated mass of ^{187}Bi (see sect. 4.2). Thus, it is not so clear if the $1/2^+$ state in astatine isotopes continues the downward trend as it does in

bismuth isotopes or whether it starts to level off near the mid-shell region (see fig. 13).

4.3.5 The $13/2^+$ state

The general behaviour of the $13/2^+$ state in odd-mass astatine isotopes resembles the behaviour of the corresponding $13/2^+$ state in odd-mass bismuth isotopes. The new result for the excitation energy of the $13/2^+$ state in ^{193}At follows the corresponding systematics in bismuth isotopes in fig. 13.

The $13/2^+$ state has not been observed in ^{195}At so far, but fig. 13 offers a possibility to estimate the excitation energy and the decay properties of this state. It can be assumed that the $13/2^+$ state would lie approximately 280 keV and 250 keV above the $1/2^+$ ground state and the $7/2^-$ state in ^{195}At, respectively. If the $9/2^-$ state lies above the $13/2^+$ state as can be estimated from fig. 13, the most probable decay modes of the $13/2^+$ state would be an $E3$ transition to the $7/2^-$ state and an alpha-decay to the corresponding $13/2^+$ state in ^{191}Bi. By using the excitation energy of 429 keV reported for the $13/2^+$ state in ^{191}Bi [61] and the results of the present work, the alpha-decay energy of the $13/2^+$ state in ^{195}At to the corresponding $13/2^+$ state in ^{191}Bi would be approximately $E_\alpha = 7045$ keV. The alpha-decay energy corresponds to a half-life of approximately 168 ms if an unhindered alpha-decay with a hindrance factor equal to unity is assumed. Correspondingly, the Weisskopf estimate for a 250 keV $E3$ transition from the $13/2^+$ state to the $7/2^-$ state in ^{195}At corrected for internal conversion is $T_{1/2} = 3$ ms. In addition, it can be assumed that the strength of the $E3$ transition would be approximately 3 W.u., as deduced for the corresponding transition in ^{193}At in sect. 3.1.4 (see also sect. 4.3.2 above). This would mean that the branch of the alpha-decay from the $13/2^+$ state would be too small for the detection in ^{195}At. Even if the $13/2^+$ state laid only 30 keV above the $7/2^-$ state, the $E3$ transition would be approximately 20 times faster than the alpha-decay to the $13/2^+$ state in ^{191}Bi. In addition, the alpha-decay energies of the other states could obscure this tiny alpha-decay branch. In that case, observation of the subsequent gamma-rays from the $13/2^+$ final state in ^{191}Bi ($E_\gamma = 429$ keV [61]) would be needed to ensure that the preceding alpha-decay originated from the $13/2^+$ state in ^{195}At (see the corresponding situation for ^{193}At in sect. 3.1.2). In ^{193}At the alpha-decay energy of the $13/2^+$ state is not obscured by the alpha-decay energies of the other states, as can be seen in fig. 2.

Observation and identification of the possible $E3$ transition between the $13/2^+$ and $7/2^-$ states will also be a great challenge if the half-life of the transition is of the order of 1 ms or longer. The task would be easier if the $9/2^-$ state would lie below the $13/2^+$ state. Thus, the deexcitation of the $13/2^+$ state could proceed via the $9/2^-$ state to the $7/2^-$ state with the gamma-ray transition half-lives well below 1 μs.

The possible alpha-decay energy of 7446(25) keV from the $13/2^+$ state in ^{191}At (see sect. 3.2.3) to the 252 keV excited $13/2^+$ state in ^{187}Bi [51] would indicate that the excitation energy of the $13/2^+$ state in ^{191}At would be 30(30) keV. This would mean that the $13/2^+$ state would lie even below the $7/2^-$ state in ^{191}At. However, it should be remembered that this speculation is based on only one decay chain. More statistics is needed for further discussion.

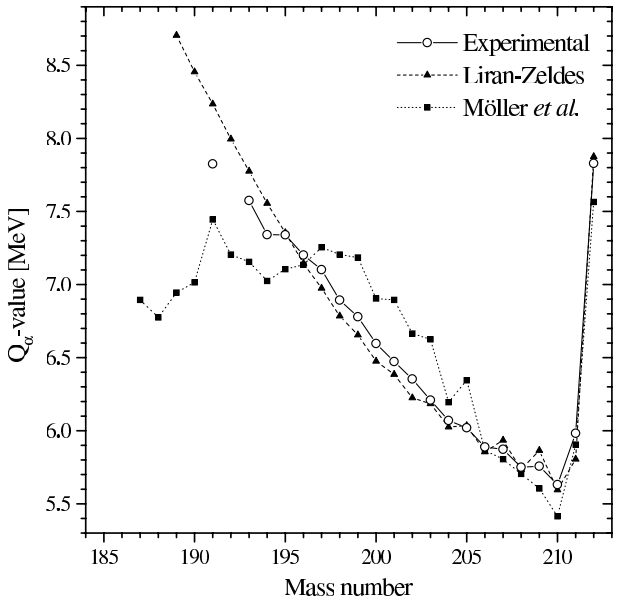

Fig. 14. Q_α values for neutron-deficient astatine isotopes. The open circles represent experimental data, including the Q_α values of ^{191}At and ^{193}At determined in the present work. The filled triangles and squares represent Q_α values calculated using the mass tables of Liran and Zeldes [67] and Möller *et al.* [9], respectively.

4.3.6 Q_α values and proton separation energies

In fig. 14 the experimental alpha-decay Q_α values of astatine isotopes, including the Q_α values for ^{191}At and ^{193}At obtained in the present work, are shown along with the values calculated using the mass tables of Liran and Zeldes [67] and Möller *et al.* [9]. The experimental data presented for heavier astatine isotopes were taken from refs. [33,24,46].

The alpha-decay Q_α values obtained using the results of the semiempirical shell-model formula of Liran and Zeldes fit rather well to the experimental results. In light astatine isotopes the formula overestimates the alpha-decay Q_α values, since the systematic increase of the experimental Q_α values slows down after ^{197}At, as can be seen in fig. 14. In odd-mass isotopes the slowing-down is due to the change of the character of the ground state between ^{197}At and ^{195}At from a spherical $9/2^-$ state to a slightly oblate $1/2^+$ state, while the daughter nuclei stay almost spherical. In ^{194}At the drop in the experimental alpha-decay Q_α value [33] compared to the systematics trend is even larger. This may indicate a similar change in the ground-state structure of even-mass astatine

isotopes as observed in odd-mass astatine isotopes. However, it should be remembered that the alpha-decay properties of ^{194}At are not very well known.

The alpha-decay Q_α values obtained using the results of the macroscopic-microscopic calculation of Möller *et al.* [9] differ considerably from the experimental results. In the heavier astatine isotopes the increase in the alpha-decay Q_α values with decreasing mass number is overestimated up to ^{199}At. After ^{199}At the alpha-decay Q_α value stays almost constant until there is a slight increase in ^{191}At and then a decrease again. These changes in the systematic trends of the calculated alpha-decay Q_α values occur in the places where the quadrupole deformation of the astatine isotopes were predicted (by Möller *et al.*) to change from nearly spherical in ^{199}At with $\beta_2 = 0.08$ to an oblate in ^{198}At with $\beta_2 = -0.21$ and from oblate ^{191}At with $\beta_2 = -0.22$ to prolate ^{190}At with $\beta_2 = 0.3$, while the daughter nuclei (bismuth) were predicted to stay almost spherical [9].

Figure 15 shows the proton separation energies for odd-mass Ir, Au, Tl, Bi, At, Fr and Ac isotopes. The negative separation energies indicate that the nucleus is not proton bound compared to the ground state of the daughter nucleus (compare to fig. 12). The filled circles denote energies derived from the measured atomic masses presented in refs. [57,31], except the points shown for Ac and Fr isotopes and for Tl, Au and Ir isotopes below the dotted line. Masses for these proton separation energies were taken from ref. [30], which contains measured and also extrapolated atomic masses. The open circles represent the measured proton separation energies for ground-state–to–ground-state proton decays [68,69]. Correspondingly, the open triangles represent the measured proton separation energies, but in these cases the proton decays most probably originate from excited states [25,26].

As can be seen in fig. 15, the use of the extrapolated masses of ref. [30] tend to overestimate the decrease of the proton separation energy, especially in Au and Tl isotopes. In light Tl isotopes the systematics of the separation energy behaves unexpectedly when the measured point is taken into account. In bismuth and astatine isotopes the masses for ^{187}Bi and ^{191}At are not well known. For these nuclei the masses approximated in sect. 4.2 were used.

The proton separation energies of astatine isotopes decrease smoothly with decreasing mass number until the first clearly proton-unbound isotope ^{195}At [24] is reached. The graph behaves as if the two curves would cross between ^{197}At and ^{195}At. This is indeed true, since the ground-state change from a $9/2^-$ state to a $1/2^+$ state (see fig. 12) causes the bend in the proton separation energy systematics. A similar, but weaker, behaviour can also be seen in bismuth isotopes (see sect. 4.3.1). Proton separation energies of approximately -560 keV and -1020 keV can be estimated for ^{193}At and ^{191}At, respectively. For ^{191}At this would correspond to a partial half-life of approximately 57 s for an unhindered proton decay from the $\pi s_{1/2}$ orbital. This is calculated using the WKB barrier transmission approximation through the real part of a Becchetti-Greenlees optical potential [70]. Although the WKB approximation is very rough and works mainly for spherical nuclei, it shows that the branching ratio of the proton decay compared to the alpha-decay with a half-life $T_{1/2} = (1.7^{+1.1}_{-0.5})$ ms would be too small for detection, especially if the spectroscopic factor of the proton decay is taken into account in the half-life approximation. By extrapolating the systematics of the proton separation energies of the astatine isotopes, it can be estimated that the proton separation energy of the next odd-mass astatine isotope ^{189}At would be approximately -1500 keV, which would surely be negative enough for proton decay to compete successfully with alpha-decay.

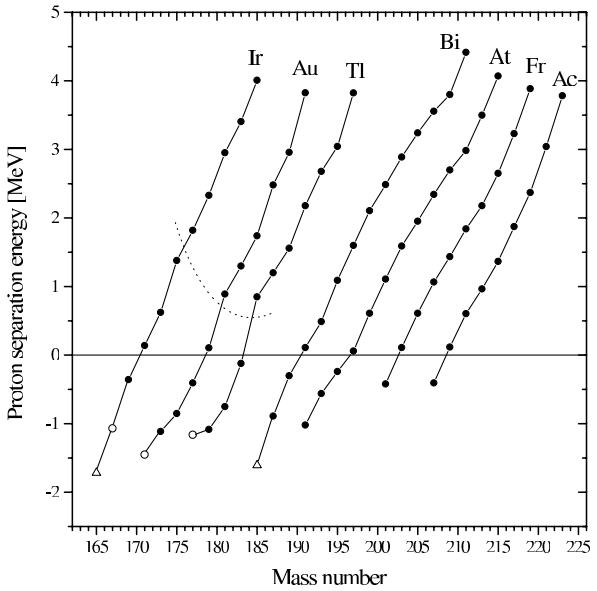

Fig. 15. Proton separation energies for odd-mass Ir, Au, Tl, Bi, At, Fr and Ac isotopes. The filled circles denote energies derived from the measured atomic masses presented in refs. [57,31], except for Ac and Fr isotopes and for Tl, Au and Ir isotopes below the dotted line the masses presented in ref. [30] were used. The open circles represent the measured proton separation energies for the ground-state–to–ground-state proton decays [68,69]. The open triangles represent the measured proton separation energies, but in these cases the proton decay most probably originates from an excited state [25,26].

5 Conclusion

The alpha-decay properties of the new isotope ^{191}At were investigated for the first time and the decay properties of ^{193}At were studied with improved accuracy. New information about the corresponding daughter nuclei ^{187}Bi and ^{189}Bi was also obtained.

Three alpha-decaying states were identified for ^{193}At and two for ^{191}At. In both isotopes the $1/2^+$ intruder state was determined as the ground state, though in ^{193}At also the $7/2^-$ state with 5(10) keV excitation energy could represent the ground state within the accuracy of the measurement. The alpha-decay of the excited $7/2^-$ state in ^{193}At was observed to feed an excited $7/2^-$ state at

99.6(5) keV in ^{189}Bi. The spin, parity and excitation energy of the final state in bismuth were determined using the properties of gamma-ray transitions observed in coincidence with the alpha-decay of ^{193}At. Identification of the $13/2^+$ state in ^{193}At was also based on the alpha-gamma coincidences. In ^{187}Bi the existence of the excited $7/2^-$ state at 63(10) keV was deduced from the shape of the alpha-decay energy spectrum of ^{191}At and the systematics observed in the heavier odd-mass bismuth isotopes. A possible observation of the alpha-decay from $13/2^+$ state in ^{191}At was also discussed. The unhindered alpha-decays to the final states in bismuth were used to determine the assignments of the initial states in ^{191}At and ^{193}At isotopes.

The level schemes obtained for ^{191}At and ^{193}At in the present work are similar to the previous level scheme of ^{195}At, which was suggested to differ from those observed in the heavier odd-mass astatine isotopes. It was also proposed that the deformed three-particle configuration, driving the last proton to the $7/2^-[514]$ Nilsson state, is energetically more favoured than the nearly spherical $(\pi h_{9/2})^3$ configuration in these light ($A < 197$) odd-mass astatine isotopes. The existence of the corresponding low-lying $7/2^-$ state in bismuth isotopes was also explained by the single-particle $7/2^-[514]$ Nilsson proton state.

Finally, the proton binding energies of the odd-mass bismuth and astatine isotopes were discussed. Based on the observed systematics, it was predicted that the next odd-mass astatine isotope ^{189}At would be a potential candidate for the observation of proton emission.

The crossing of the $1/2^+$ and $7/2^-$ states with the $9/2^-$ state in ^{197}At was observed as a bend in the proton binding energy systematics. The bend can be understood by the crossing of two different nuclear shapes. The $9/2^-$ state is associated with the spherical shape and the $1/2^+$ and $7/2^-$ states are associated with the slightly oblate shape. It was surprising that a similar bend was observed in bismuth isotopes. In analogy to astatine isotopes it may indicate a change also in the structure of bismuth isotopes. In future the comparison of the precise nuclear-mass information with the ground-state deformation information will be very interesting if it is true that the changes in ground-state deformation could be seen also in the systematics of the ground-state masses.

This work was supported by the Academy of Finland under the Finnish Centre of Excellence Programme 2002-2005 (Project No. 44875, Nuclear and Condensed Matter Physics Programme at JYFL). A.K. would like to acknowledge financial support provided by a Marie Curie Fellowship of the European Community program "Improving Human Research Potential and the Socio-economic Knowledge Base" Contract No. HPMF-CT-2000-01115.

References

1. J.L. Wood, K. Heyde, W. Nazarewicz, M. Huyse, P. Van Duppen, Phys. Rep. **215**, 101 (1992).
2. F.R. May, V.V. Pashkevich, S. Frauendorf, Phys. Lett. B **68**, 113 (1977).
3. R. Bengtsson, W. Nazarewicz, Z. Phys. A **334**, 269 (1989).
4. R.G. Allatt, R.D. Page, M. Leino, T. Enqvist, K. Eskola, P.T. Greenlees, P. Jones, R. Julin, P. Kuusiniemi, W.H. Trzaska, J. Uusitalo, Phys. Lett. B **437**, 29 (1998).
5. A.N. Andreyev, M. Huyse, P. Van Duppen, L. Weissman, D. Ackermann, J. Gerl, F.P. Heßberger, S. Hofmann, A. Kleinböhl, G. Münzenberg, S. Reshitko, C. Schlegel, H. Schaffner, P. Cagarda, M. Matos, S. Saro, A. Keenan, C. Moore, C.D. O'Leary, R.D. Page, M. Taylor, H. Kettunen, M. Leino, A. Lavrentiev, R. Wyss, K. Heyde, Nature **405**, 430 (2000).
6. K. Helariutta, J.F.C. Cocks, T. Enqvist, P.T. Greenlees, P. Jones, R. Julin, S. Juutinen, P. Jämsen, H. Kankaanpää, H. Kettunen, P. Kuusiniemi, M. Leino, M. Muikku, M. Piiparinen, P. Rahkila, A. Savelius, W.H. Trzaska, S. Törmänen, J. Uusitalo, R.G. Allatt, P.A. Butler, R.D. Page, M. Kapusta, Eur. Phys. J. A **6**, 289 (1999).
7. K. Van de Vel, A.N. Andreyev, R.D. Page, H. Kettunen, P.T. Greenlees, P. Jones, R. Julin, S. Juutinen, H. Kankaanpää, A. Keenan, P. Kuusiniemi, M. Leino, M. Muikku, P. Nieminen, P. Rahkila, J. Uusitalo, K. Eskola, A. Hürstel, M. Huyse, Y. Le Coz, M.B. Smith, P. Van Duppen, R. Wyss, Eur. Phys. J. A **17**, 167 (2003).
8. A.N. Andreyev, D. Ackermann, P. Cagarda, J. Gerl, F. Heßberger, S. Hofmann, M. Huyse, A. Keenan, H. Kettunen, A. Kleinböhl, A. Lavrentiev, M. Leino, B. Lommel, M. Matos, G. Münzenberg, C. Moore, C.D. O'Leary, R.D. Page, S. Reshitko, S. Saro, C. Schlegel, H. Schaffner, M. Taylor, P. Van Duppen, L. Weissman, R. Wyss, Eur. Phys. J. A **6**, 381 (1999).
9. P. Möller, J.R. Nix, W.D. Myers, W.J. Swiatecki, At. Data Nucl. Data Tables **59**, 185 (1995).
10. R. Bengtsson, P. Möller, J.R. Nix, Jing-ye Zhang, Phys. Scr. **29**, 402 (1984).
11. R.S. Simon, K.-H. Schmidt, F.P. Heßberger, S. Hlavac, M. Housek, G. Münzenberg, H.-G. Clerc, U. Gollerthan, W. Schwab, Z. Phys. A **325**, 197 (1986).
12. E.S. Paul, P.J. Woods, T. Davinson, R.D. Page, P.J. Sellin, C.W. Beausang, R.M. Clark, R.A. Cunningham, S.A. Forbes, D.B. Fossan, A. Gizon, J. Gizon, K. Hauschild, I.M. Hibbert, A.N. James, D.R. LaFosse, I. Lazarus, H. Schnare, J. Simpson, R. Wadsworth, M.P. Waring, Phys. Rev. C **51**, 78 (1995).
13. R.B. Taylor, S.J. Freeman, J.L. Durrell, M.J. Leddy, S.D. Robinson, B.J. Varley, J.F.C. Cocks, K. Helariutta, P. Jones, R. Julin, S. Juutinen, H. Kankaanpää, A. Kanto, H. Kettunen, P. Kuusiniemi, M. Leino, M. Muikku, P. Rahkila, A. Savelius, P.T. Greenlees, Phys. Rev. C **59**, 673 (1999).
14. R.B. Taylor, S.J. Freeman, J.L. Durrell, M.J. Leddy, A.G. Smith, D.J. Blumenthal, M.P. Carpenter, C.N. Davids, C.J. Lister, R.V.F. Janssens, D. Seweryniak, Phys. Rev. C **54**, 2926 (1996).
15. S.J. Freeman, A.G. Smith, S.J. Warburton, B.B. Back, I.G. Bearden, D.J. Blumenthal, M.P. Carpenter, B. Crowell, C.N. Davids, D. Henderson, R.V.F. Janssens, T.L. Khoo, T. Lauritsen, C.J. Lister, D. Nisius, H.T. Penttilä, J.A. Becker, P. Chowdhury, E.F. Moore, Phys. Rev. C **50**, R1754 (1994).
16. D. Horn, C. Baktash, C.J. Lister, Phys. Rev. C **24**, 2136 (1981).

17. D.J. Dobson, S.J. Freeman, P.T. Greenlees, A.N. Qadir, S. Juutinen, J.L. Durell, T. Enqvist, P. Jones, R. Julin, A. Keenan, H. Kettunen, P. Kuusiniemi, M. Leino, P. Nieminen, P. Rahkila, S.D. Robinson, J. Uusitalo, B.J. Varley, Phys. Rev. C **66**, 064321 (2002).
18. T.P. Sjoreen, G. Schatz, S.K. Bhattacherjee, B.A. Brown, D.B. Fossan, P.M.S. Lesser, Phys. Rev. C **14**, 1023 (1976).
19. T.P. Sjoreen, U. Garg, D.B. Fossan, Phys. Rev. C **23**, 272 (1981).
20. T.P. Sjoreen, D.B. Fossan, U. Garg, A. Neskakis, A.R. Poletti, E.K. Warburton, Phys. Rev. C **25**, 889 (1982).
21. K. Dybdal, T. Chapuran, D.B. Fossan, W.F. Piel, D. Horn, E.K. Warburton, Phys. Rev. C **28**, 1171 (1983).
22. M. Lach, P. Bednarczyk, P.T. Greenlees, K. Helariutta, P. Jones, R. Julin, S. Juutinen, H. Kankaanpää, H. Kettunen, P. Kuusiniemi, M. Leino, W. Męczyński, M. Muikku, P. Nieminen, P. Rahkila, J. Styczeń, J. Uusitalo, Eur. Phys. J. A **9**, 307 (2000).
23. M.B. Smith, R. Chapman, J.F.C. Cocks, O. Dorvaux, K. Helariutta, P. Jones, R. Julin, S. Juutinen, H. Kankaanpää, H. Kettunen, P. Kuusiniemi, Y. Le Coz, M. Leino, D.J. Middleton, M. Muikku, P. Nieminen, P. Rahkila, A. Savelius, K.-M. Spohr, Eur. Phys. J. A **5**, 43 (1999).
24. H. Kettunen, T. Enqvist, M. Leino, K. Eskola, P.T. Greenlees, K. Helariutta, P. Jones, R. Julin, S. Juutinen, H. Kankaanpää, H. Koivisto, P. Kuusiniemi, M. Muikku, P. Nieminen, P. Rahkila, J. Uusitalo, Eur. Phys. J. A **16**, 457 (2003).
25. C.N. Davids, P.J. Woods, H.T. Penttilä, J.C. Batchelder, C.R. Bingham, D.J. Blumenthal, L.T. Brown, B.C. Busse, L.F. Conticchio, T. Davinson, D.J. Henderson, R.J. Irvine, D. Seweryniak, K.S. Toth, W.B. Walters, B.E. Zimmerman, Phys. Rev. Lett. **76**, 592 (1996).
26. G.L. Poli, C.N. Davids, P.J. Woods, D. Seweryniak, M.P. Carpenter, J.A. Cizewski, T. Davinson, A. Heinz, R.V.F. Janssens, C.J. Lister, J.J. Ressler, A.A. Sonzogni, J. Uusitalo, W.B. Walters, Phys. Rev. C **63**, 044304 (2001).
27. Sven Åberg, Paul B. Semmes, Witold Nazarewicz, Phys. Rev. C **56**, 1762 (1997).
28. C.N. Davids, P.J. Woods, D. Seweryniak, A.A. Sonzogni, J.C. Batchelder, C.R. Bingham, T. Davinson, D.J. Henderson, R.J. Irvine, G.L. Poli, J. Uusitalo, W.B. Walters, Phys. Rev. Lett. **80**, 1849 (1998).
29. Cary N. Davids, Henning Esbensen, Phys. Rev. C **61**, 054302 (2000).
30. G. Audi, O. Bersillon, J. Blachot, A.H. Wapstra, Nucl. Phys. A **624**, 1 (1997).
31. Yu.N. Novikov, F. Attallah, F. Bosch, M. Falch, H. Geissel, M. Hausmann, Th. Kerscher, O. Klepper, H.-J. Kluge, C. Kozhuharov, Yu.A. Litvinov, K.E.G. Löbner, G. Münzenberg, Z. Patyk, T. Radon, C. Scheidenberger, A.H. Wapstra, H. Wollnik, Nucl. Phys. A **697**, 92 (2002).
32. T. Enqvist, thesis (Department of Physics, University of Jyväskylä, Research Report No. 3/1996), unpublished.
33. M. Leino, J. Äystö, T. Enqvist, A. Jokinen, M. Nurmia, A. Ostrowski, W.H. Trzaska, J. Uusitalo, K. Eskola, P. Armbruster, V. Ninov, Acta Phys. Pol. B **26**, 309 (1995).
34. H. Koivisto, J. Ärje, M. Nurmia, Nucl. Instrum. Methods Phys. Res. B **94**, 291 (1994).
35. J.F. Ziegler, J.P. Biersack, U. Littmark, *The Stopping and Range of Ions in Solids*, new edition (Pergamon, New York, 1999).
36. M. Leino, J. Äystö, T. Enqvist, P. Heikkinen, A. Jokinen, M. Nurmia, A. Ostrowski, W.H. Trzaska, J. Uusitalo, P. Armbuster, V. Ninov, Nucl. Instrum. Methods Phys. Res. B **99**, 653 (1995).
37. H. Kettunen, P.T. Greenlees, K. Helariutta, P. Jones, R. Julin, S. Juutinen, P. Kuusiniemi, M. Leino, M. Muikku, P. Nieminen, J. Uusitalo, Acta Phys. Pol. B **32**, 989 (2001).
38. H. Kettunen *et al.*, in preparation.
39. A. Rytz, At. Data Nucl. Data Tables **47**, 205 (1991).
40. A.N. Andreyev, N. Bijnens, T. Enqvist, M. Huyse, P. Kuusiniemi, M. Leino, W.H. Trzaska, J. Uusitalo, P. Van Duppen, Z. Phys. A **358**, 63 (1997).
41. J. Wauters, P. Dendooven, M. Huyse, G. Reusen, P. Van Duppen, Phys. Rev. C **47**, 1447 (1993).
42. A.N. Andreyev, M. Huyse, P. Van Duppen, J.F.C. Cocks, K. Helariutta, H. Kettunen, P. Kuusiniemi, M. Leino, W.H. Trzaska, K. Eskola, R. Wyss, Phys. Rev. Lett. **82**, 1819 (1999).
43. K.-H. Schmidt, C.-C. Sahm, K. Pielenz, H.-G. Clerc, Z. Phys. A **316**, 19 (1984).
44. K.-H. Schmidt, Eur. Phys. J. A **8**, 141 (2000).
45. P. Van Duppen, P. Decrock, P. Dendooven, M. Huyse, G. Reusen, J. Wauters, Nucl. Phys. A **529**, 268 (1991).
46. R.B. Firestone, V.S. Shirley, *Table of Isotopes*, 8th edition (Wiley, New York, 1996).
47. K. Van de Vel, A.N. Andreyev, M. Huyse, P. Van Duppen, J.F.C. Cocks, O. Dorvaux, P.T. Greenlees, K. Helariutta, P. Jones, R. Julin, S. Juutinen, H. Kettunen, P. Kuusiniemi, M. Leino, M. Muikku, P. Nieminen, K. Eskola, R. Wyss, Phys. Rev. C **65**, 064301 (2002).
48. J. Wauters, J.C. Batchelder, C.R. Bingham, D.J. Blumenthal, L.T. Brown, L F. Conticchio, C.N. Davids, T. Davinson, R.J. Irvine, D. Seweryniak, K.S. Toth, W.B. Walters, P.J. Woods, E.F. Zganjar, Phys. Rev. C **55**, 1192 (1997).
49. J.O. Rasmussen, Phys. Rev. **113**, 1593 (1959).
50. A.N. Andreyev, D. Ackermann, P. Cagarda, J. Gerl, F.P. Heßberger, S. Hofmann, M. Huyse, A. Keenan, H. Kettunen, A. Kleinböhl, A. Lavrentiev, M. Leino, B. Lommel, M. Matos, G. Münzenberg, C.J. Moore, C.D. O'Leary, R.D. Page, S. Reshitko, S. Saro, C. Schlegel, H. Schaffner, M.J. Taylor, P. Van Duppen, L. Weissman, R. Wyss, Eur. Phys. J. A **10**, 129 (2001).
51. A. Hürstel, M. Rejmund, E. Bouchez, P.T. Greenlees, K. Hauschild, S. Juutinen, H. Kettunen, W. Korten, Y. Le Coz, P. Nieminen, Ch. Theisen, A.N. Andreyev, F. Becker, T. Enqvist, P.M. Jones, R. Julin, H. Kankaanpää, A. Keenan, P. Kuusiniemi, M. Leino, A.-P. Leppänen, M. Muikku, J. Pakarinen, P. Rahkila, J. Uusitalo, Eur. Phys. J. A **15**, 329 (2002).
52. J. Kantele, *Handbook of Nuclear Spectrometry* (Academic Press, London, 1995).
53. P.A. Butler, programmed in April 1998, private communication.
54. H. Kettunen *et al.*, in preparation.
55. J.C. Batchelder, K.S. Toth, C.R. Bingham, L.T. Brown, L.F. Conticchio, C.N. Davids, R.J. Irvine, D. Seweryniak, W.B. Walters, J. Wauters, E.F. Zganjar, J.L. Wood, C. DeCoster, B. Decroix, K. Heyde, Eur. Phys. J. A **5**, 49 (1999).
56. P. Möller, J.R. Nix, K.-L. Kratz, At. Data Nucl. Data Tables **66**, 131 (1997).

57. T. Radon, H. Geissel, G. Münzenberg, B. Franzke, Th. Kerscher, F. Nolden, Yu.N. Novikov, Z. Patyk, C. Scheidenberger, F. Attallah, K. Beckert, T. Beha, F. Bosch, H. Eickhoff, M. Falch, Y. Fujita, M. Hausmann, F. Herfurth, H. Irnich, H.C. Jung, O. Klepper, C. Kozhuharov, Yu.A. Litvinov, K.E.G. Löbner, F. Nickel, H. Reich, W. Schwab, B. Schlitt, M. Steck, K. Sümmerer, T. Winkler, H. Wollnik, Nucl. Phys. A **677**, 75 (2000).
58. E. Coenen, K. Deneffe, M. Huyse, P. Van Duppen, J.L. Wood, Z. Phys. A **324**, 485 (1986).
59. W. Męczyński, P. Bednarczyk, R. Chapman, S. Courtin, J. Gręboszc, F. Hannachi, P. Jones, J. Kownacki, M. Lach, A. Lopez-Martens, K.H. Maier, J.C. Merdinger, D. Middleton, M. Palacz, M.B. Smith, K.M. Spohr, N. Schulz, M. Zięblińskii, J. Styczeń, Eur. Phys. J. A **3**, 311 (1998).
60. E. Coenen, K. Deneffe, M. Huyse, P. Van Duppen, J.L. Wood, Phys. Rev. Lett. **54**, 1783 (1985).
61. P. Nieminen, J.F.C. Cocks, O. Dorvaux, P.T. Greenlees, K. Helariutta, P.M. Jones, R. Julin, S. Juutinen, H. Kankaanpää, H. Kettunen, P. Kuusiniemi, M. Leino, M. Muikku, P. Rahkila, A. Savelius, J. Uusitalo, A.N. Andreyev, F. Becker, K. Eskola, K. Hauschild, M. Houry, M. Huyse, W. Korten, Y. Le Coz, R. Lucas, T. Lönnroth, Ch. Theisen, K. Van de Vel, P. Van Duppen, N. Amzal, P.A. Butler, N. Hammond, C. Scholey, R. Wyss, Acta Phys. Pol. B **32**, 1019 (2001).
62. A. Bohr, B.R. Mottelson, *Nuclear Structure*, Vol. **II** (World Scientific Publishing Co. Pte. Ltd., Singapore, 1998) p. 566.
63. I. Bergström, B. Fant, Phys. Scr. **31**, 26 (1985).
64. G.D. Dracoulis, T. Kibédi, A.P. Byrne, A.M. Baxter, S.M. Mullins, R.A. Bark, Phys. Rev. C **63**, 061302(R) (2001).
65. C. Ellengaard, R. Julin, J. Kantele, M. Luontama, T. Poikolainen, Nucl. Phys. A **302**, 125 (1978).
66. Richard F. Casten, *Nuclear Structure from a Simple Perspective*, second edition (Oxford University Press Inc., New York, 2000) p. 367.
67. S. Liran, N. Zeldes, At. Data Nucl. Data Tables **17**, 431 (1976).
68. C.N. Davids, P.J. Woods, J.C. Batchelder, C.R. Bingham, C.J. Blumenthal, L.T. Brown, B.C. Busse, L.F. Conticchio, T. Davinson, S.J. Freeman, D.J. Henderson, R.J. Irvine, R.D. Page, H.T. Penttilä, D. Seweryniak, K.S. Toth, W.B. Walters, B.E. Zimmerman, Phys. Rev. C **55**, 2255 (1997).
69. G.L. Poli, C.N. Davids, P.J. Woods, D. Seweryniak, J.C. Batchelder, L.T. Brown, C.R. Bingham, M.P. Carpenter, L.F. Conticchio, T. Davinson, J. DeBoer, S. Hamada, D.J. Henderson, R.J. Irvine, R.V.F. Janssens, H.J. Maier, L. Müller, F. Soramel, K.S. Toth, W.B. Walters, J. Wauters, Phys. Rev. C **59**, R2979 (1999).
70. F.D. Becchetti, G.W. Greenlees, Phys. Rev. **182**, 1190 (1969).